Review article

Raphaël Butté* and Nicolas Grandjean

# III-nitride photonic cavities

https://doi.org/10.1515/nanoph-2019-0442
Received October 25, 2019; revised December 12, 2019; accepted December 13, 2019

**Abstract:** Owing to their wide direct bandgap tunability, III-nitride (III-N) compound semiconductors have been proven instrumental in the development of blue light-emitting diodes that led to the so-called solid-state lighting revolution and blue laser diodes that are used for optical data storage. Beyond such conventional optoelectronic devices, in this review, we explore the progress made in the past 15 years with this low refractive index material family for the realization of microdisks as well as 2D and 1D photonic crystal (PhC) membrane cavities. Critical aspects related to their design and fabrication are first highlighted. Then, the optical properties of passive PhC structures designed for near-infrared such as their quality factor and their mode volume are addressed. Additional challenges dealing with fabrication pertaining to structures designed for shorter wavelengths, namely the visible to ultraviolet spectral range, are also critically reviewed and analyzed. Various applications ranging from second and third harmonic generation to microlasers and nanolasers are then discussed. Finally, forthcoming challenges and novel fields of application of III-N photonic cavities are commented.

**Keywords:** III-nitrides; photonic crystal; microdisk.

## 1 Introduction

In the past 20 years, III-nitride (III-N) compound semiconductors have become part of our daily life, as they are at the heart of the solid-state lighting revolution. Indeed, they lie behind the development of blue to green light-emitting diodes and laser diodes that are ubiquitous devices nowadays [1–3]. Beyond such conventional optoelectronic devices, the III-N semiconductor family has already proven to be rather versatile and unique, as it possesses numerous assets for expanding areas of nanophotonics that can otherwise hardly be addressed by a single material family. First, thanks to their wide bandgap (up to ~6.0 eV at 300 K for the strain-free AlN compound [4]), the accessible spectral window for optical resonators made from III-Ns can cover regions going all the way from the ultraviolet (UV)-C region (~210 nm for the shortest accessible wavelength) down to the near-infrared (NIR) spectral range, including the optical communication wavelength bands, namely from the O-band to the L-band, which cover the 1260–1625 nm range [5]. Being compound semiconductors, these low refractive index dielectric media can be grown using well-established epitaxy techniques such as metalorganic vapor phase epitaxy and molecular beam epitaxy (MBE) to fabricate passive resonators or active ones embedding precisely positioned light-emitting and/or absorbing quantum heterostructures, most commonly quantum wells (QWs) or quantum dots (QDs), whose spectral features can be tuned over a broad range via both alloying and quantum engineering. Sputtering has also proven to be ideally suited for NIR applications relying on low-loss AlN waveguides (WGs) and microring resonators [6] that can exhibit both second- and third-order optical nonlinearities for frequency conversion and frequency comb generation. A second important asset of III-Ns for nanophotonic applications relies on their large oscillator strength and exciton binding energy, which fosters strong light-matter interaction phenomena. This is best exemplified by the report of room temperature polariton lasing in both bulk and multiple QW planar microcavities more than a decade ago [7, 8]. The large exciton binding energy of III-Ns has also been recently exploited to demonstrate single-photon emission (SPE) at room temperature from site-controlled GaN/Al(Ga)N QDs embedded in a nanowire [9]. Such features illustrate the potential of III-Ns to bring cavity quantum electrodynamics (CQED) up to ambient temperature, a flourishing research field in which specially designed cavities providing a large quality factor ($Q$) to effective mode volume ($V_m$) ratio host precisely positioned SPEs that can potentially be tuned independently to harness quantum optical features at

***Corresponding author: Raphaël Butté,** Institute of Physics, École Polytechnique Fédérale de Lausanne (EPFL), CH-1015 Lausanne, Switzerland, e-mail: raphael.butte@epfl.ch.
https://orcid.org/0000-0002-8474-217X
**Nicolas Grandjean:** Institute of Physics, École Polytechnique Fédérale de Lausanne (EPFL), CH-1015 Lausanne, Switzerland

the single photon-single quantum emitter level. In this respect, the recent report of triggered SPE in the telecom range at 300 K from point defects in GaN [10] clearly opens up new opportunities for CQED in this technologically important spectral window. Combined with *n*- and *p*-type doping capabilities and even the recent development of tunnel junctions, which hence enable efficient lateral current spreading [11], small footprint electrically driven III-N nanophotonic resonators with embedded single-photon sources for ambient temperature CQED applications truly appear to be within reach. In addition to the above-mentioned aspects, III-N nanocavities recently revealed their potential for investigating coherent light emitters operating at the few-photon level [12–14] with foreseeable applications for photonic integrated circuits (PICs) or lab-on-a-chip light sources. Owing to their biocompatibility and their reduced invasiveness, III-N nanoresonators could also offer promising perspectives in the field of optogenetics where cellular activity can be manipulated on-demand by exploiting the sensitivity of engineered proteins to blue and green photons [15].

This wide range of topics demonstrates that III-Ns can serve as a suitable toolbox to propel nanophotonics toward novel frontiers. In this respect, in this review, we will focus on small footprint high $\frac{Q}{V_m}$ ratio III-N photonic structures of the air-clad type that have experienced a fast growing development in the past 15 years, i.e. since the first reports of microdisks [16] and photonic crystal (PhC) membrane cavities [17] by Evelyn L. Hu et al. For the sake of consistency in the reported properties, we will on purpose restrict ourselves to two geometries, namely mushroom-type microdisk cavities with a diameter of <10 μm as well as 2D and 1D PhC cavities. Those cavities are arguably the most widely studied III-N optical resonators if one excludes planar microcavities and microring resonators that have been the subject of a recent review by Jung and Tang [6]. This review article will articulate around three main sections. First, we will provide a description of the main routes commonly adopted to fabricate III-N microresonators and nanoresonators. This will be followed by a second more substantial section that will be the core of this review and that will focus on the optical properties of the fabricated resonators. Thus, a first subsection will address their linear optical properties among which the physics governing the spectral dependence of *Q*, which is best illustrated in Figure 1. A second subsection will summarize the recent achievements about optical nonlinearities reported in NIR resonators with an emphasis on the strategies adopted to tailor second- and third-order

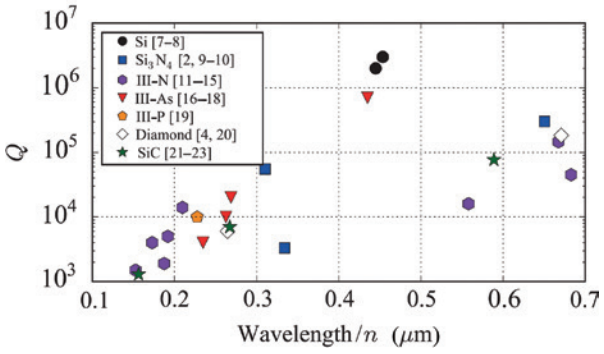


**Figure 1:** Highest reported PhC cavity *Q* for various materials plotted vs. wavelength in material, where *n* is the refractive index including dispersion.
Reprinted with permission from Ref. [18]. Copyright (2017) American Physical Society.

nonlinear processes in this noncentrosymmetric wide bandgap semiconductor family offering reduced two-photon absorption. A final subsection will review lasing features reported in air-clad III-N microdisks and PhC nanocavities. A third main section will address some forthcoming challenges facing those III-N photonic resonators. It will include pending issues about high spontaneous emission coupling factor (high-β) nanolasers such as light extraction and electrical injection but also the requirements to observe two landmarks of CQED, namely the Purcell effect – which remained elusive thus far in III-N resonators relying on a pure dielectric approach despite numerous claims, and the strong coupling regime at the single photon-single quantum emitter level. Finally, a brief summary about this field of research and an outlook will be given.

## 2 Design and fabrication of III-N microresonators and nanoresonators

Before any processing step leading to suspended III-N membranes, care should be taken regarding the WG design whatever the targeted final geometry, namely microdisks or PhCs. Indeed, one of the specificities of III-N epilayers vs. their silicon (Si) or GaAs/InP counterparts originates from the heteroepitaxial nature of the waveguiding layers, as to date there is no existing report of such microphotonic and nanophotonic resonators that were grown on polar freestanding GaN or bulk AlN substrates. Hence, the vast majority of the samples are grown on either *c*-plane sapphire or Si (111) substrates, which

is in line with their use in III-N optoelectronics. Sample growth on other substrates has also been reported, but this is often a choice specific to some research groups. In particular, this is the case for 6H-SiC (0001) substrates (see, e.g. Ref. [19] but also *m*-plane GaN [20]) or Si (001) substrates used for the growth of cubic (zinc-blende) epilayers [21], with the latter two containing nonpolar quantum heterostructures. The heteroepitaxial growth of III-N epilayers is obviously known to affect the material quality, which often translates into a high threading dislocation density (TDD), typically $\geq 10^8$ cm$^{-2}$. This can not only impair the internal quantum efficiency (IQE) of the embedded heterostructures but also increase the top and bottom WG interface roughness, hence potentially altering the measured $Q$ values of the resonators of interest due to increased scattering losses. Let us note in this respect that thin III-N WG epilayers grown on Si are expected to be much more impacted than those grown on sapphire, owing to their tensile strain nature and the much larger TDD ($\geq 10^{10}$ cm$^{-2}$).

A symmetric epilayer along the growth axis would be ideally suited to vertically confine optical modes in the central part of the WG. Although this is clearly not an issue for WG epilayers grown on *c*-plane sapphire substrates, the same statement does not hold true for GaN WGs grown on Si (111) substrates. Indeed, in this latter case, it is known that the growth of a thin AlN buffer layer, a few tens of nanometer thick, is required to prevent any destructive melt-back etching of the Si surface due to the high reactivity between Ga and Si [22]. III-N WGs can essentially be categorized in two families depending on the targeted studies, namely structures with or without embedded quantum heterostructures. In the absence of any such internal light source, III-N resonators are usually optimized for NIR operation, and in this latter case, the WG thickness is much larger than that of their UV to visible counterparts. For long-wavelength (NIR) applications, this is obviously not problematic by any means to deal with reasonably thick WGs for which the mode order ($m$) is kept to lowest order, i.e. $m=0$. However, at shorter wavelengths, preserving lowest-order operation is not necessarily given for granted, especially in the particular case of GaN WGs grown on Si (111) substrates. This can be understood by the trade-off that is required to simultaneously ensure that (i) only the two most fundamental transverse electric (TE)/transverse magnetic (TM) WG modes are present, (ii) the WG will be thick enough to have a surface roughness that is not impacted by pits, and (iii) the embedded active medium will not be plagued by the AlN/GaN interface, whose too close proximity is known to severely alter the IQE due to the presence of nonradiative defects. Knowing that $m=0$ operation requires a WG thickness on the order of $\frac{\lambda}{2n_{\text{eff}}}$, where $\lambda$ is the wavelength in surrounding air/vacuum and $n_{\text{eff}}$ is the effective refractive index of the WG, a suspended GaN WG intended for the blue spectral range ($\lambda \approx 450$ nm) should have a thickness of <93 nm using $n$ ($\lambda = 450$ nm) ~2.44 in place of $n_{\text{eff}}$ [23]. We will see that such GaN WGs grown on Si (111) substrates require an overall epilayer thickness on the order of 300 nm, including the AlN buffer layer. It therefore leads to the presence of the four most fundamental TE/TM WG modes, i.e. those having $m=0$ and 1, before any epilayer structuring.

Following those preliminary considerations, we will now address some design and fabrication/processing aspects specific to each geometry. We shall see that, despite the obvious difference in the final shape between the two types of air-clad III-N photonic resonators, they both share several common processing steps. Let us also note that the progress made in terms of processing of those microphotonic and nanophotonic structures culminates with the recent demonstrations of PICs on Si (111) substrates including either microdisks or PhC cavities coupled to a bus WG intended for either NIR [24] or visible [25] operation (Figure 2).

## 2.1 Microdisks

The mushroom-type microdisk resonator geometry is far simpler than its PhC counterpart. It was first reported at Bell Labs by McCall et al. using the InP/InGaAsP material system [26]. Since then, it has been implemented with many other dielectric platforms. As far as air-clad resonators are concerned, the absence of any suitable wet etching route for Ga-polar III-N epilayers precludes the use of soft processing approaches that have been proven successful with other inorganic semiconductor families [27]. Therefore, after sample growth, the most common method adopted to obtain small footprint III-N microdisks, i.e. small mode volume resonators supporting high-$Q$ whispering gallery modes (WGMs) that are tightly confined within the dielectric slab due to total internal reflection, usually consists of first depositing an $SiO_2$ layer by plasma-enhanced chemical vapor deposition (PECVD). This layer will subsequently act as a hard mask during the whole process and protect the (Al)GaN surface from any damage that could occur during etching steps and ensure a proper transfer of the resonator pattern. Let us note that this $SiO_2$ layer is generally removed at the very end of the fabrication process using a buffered hydrofluoric acid solution. It is

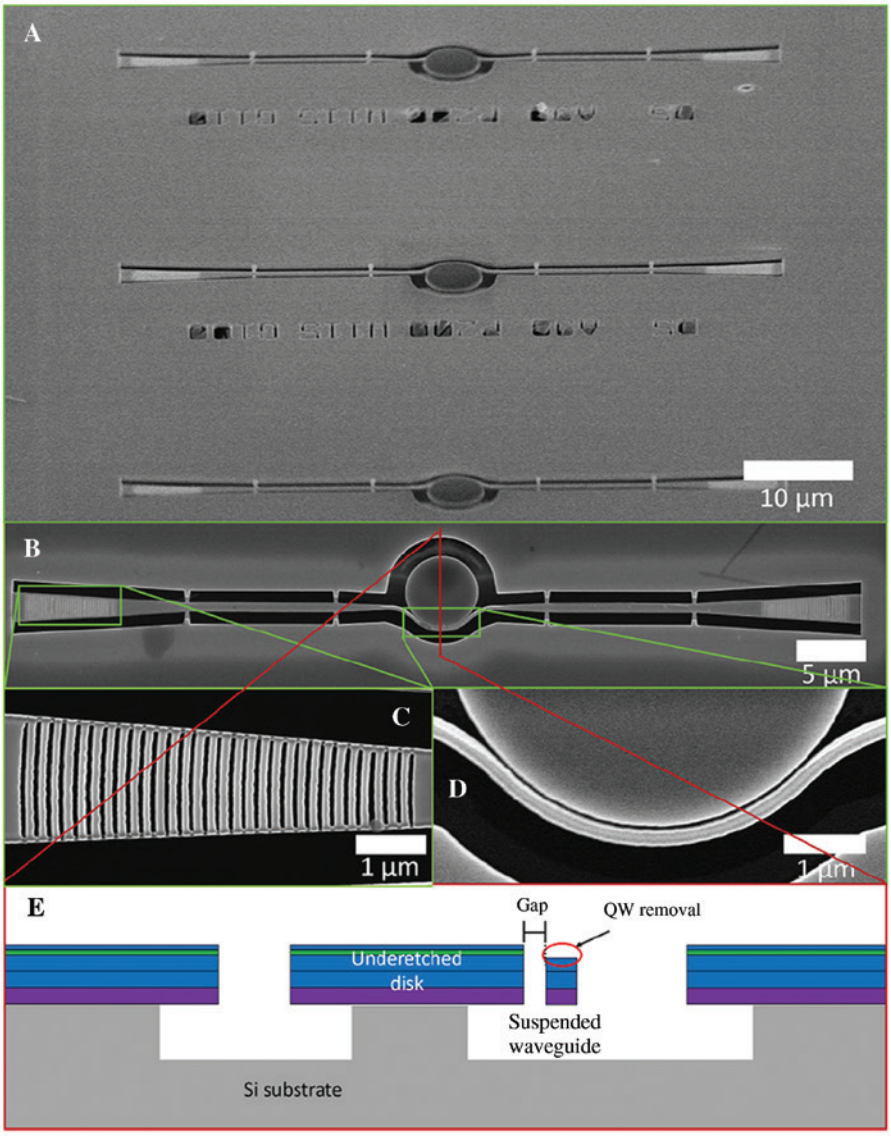


**Figure 2:** SEM image of a III-N photonic circuit.
(A) View of several devices at an angle, (B) top view of one device, (C) close-up of a grating coupler, (D) close-up of the disk and WG coupling region, and (E) sketch of a side view of the fabricated device. Reprinted with permission from Ref. [25]. Copyright (2018) American Chemical Society.

followed by spin coating of a resist, in recent years mostly dedicated to electron beam lithography (EBL) for improved spatial resolution. It is often baked to minimize any transfer of undesired defects such as sidewall roughness and striation that could incur scattering losses [28]. The most popular choice usually goes for the ZEP520A-positive resist [29], whereas the use of the UV3-positive resist remains more confidential [30]. As will be explained in detail hereafter, another recent alternative choice relies on the use of the negative tone hydrogen silsesquioxane (HSQ) EBL resist. The latter can directly be used as a hard mask [18, 31], hence allowing for a single-step pattern transfer that leads to improved fabrication and thus higher $Q$ values and higher device yield over the conventional two-step pattern transfer. After resist development, the pattern is transferred to the various layers using either reactive ion etching (RIE) or inductively coupled plasma (ICP)-RIE.

The subsequent membrane release is then determined by the nature of the host substrate. The processing of sapphire – one of the most chemically inert and hardest available oxides – being ruled out, air-clad III-N resonators fabricated from epilayers grown on this substrate are achieved by lateral etching of a sacrificial underlayer (UL) to release the membrane. The most widely used approach

consists of the selective etching of an InGaN/GaN superlattice (SL) using a photoelectrochemical (PEC) method, whereby a suitable light source, a xenon lamp whose short wavelength components (≤360 nm) are filtered out, generates most of the carriers in the sacrificial layer. It was first implemented for the realization of III-N microdisks by Haberer et al. [16]. Another successful approach for the realization of mushroom-type GaN microdisks on sapphire was based on the anodic oxidation of an InAlN UL in a basic NTA:KOH solution, which was subsequently dissolved in a heated nitric acid solution [32]. However, the downside when etching those ULs is the potential formation of defects such as whiskers in PEC etched sacrificial InGaN SL layers [33] or inverted pyramids through the nonuniform oxidation of the InAlN layer [32] that can impair the $Q$ values of WGMs.

For samples grown on Si (111) substrates, III-N epilayers are left untouched and the selective etching of the host substrate is used instead. Although RIE has been used in some occasions to release the epilayer membrane [34], the most common approach relies on chemically selective isotropic etching of Si in a pulsed $XeF_2$ vapor [35]. This is indeed a very gentle process that leaves III-N epilayers, especially the bottom N-polar face, nearly untouched [36]. One great advantage of air-clad III-N resonators fabricated on Si over sapphire stems from the possibility to achieve large air gaps, in excess of a few micrometers [34], together with a large disk diameter to post diameter ratio, hence enabling an efficient decoupling of the WGMs from the substrate. As an illustration, the scanning electron microscopy (SEM) image of a 4.0 μm GaN microdisk fabricated on Si with a reduced post diameter (~1.2 μm) using the above-mentioned single-step pattern transfer is shown in Figure 3. Such large air gaps also open access to the NIR spectral range, which remains presently unaccessible to epilayers grown on *c*-plane sapphire, and makes the realization of PICs that could be integrated to the Si photonic platform a tangible perspective. In this respect, regarding III-N microdisks that are part of PICs, the optical coupling of those resonators to the circuits is best ensured via side coupling to a suspended bus WG [25, 38–40]. In this latter case, the main challenge to overcome in terms of fabrication deals with the fine tuning of the distance between the microdisk and the WG, which will depend on the targeted applications and the desired figures of merit. Indeed, in this configuration, optical characterization is performed through transmission measurements giving access to the loaded $Q$ values ($Q_{load}$) that will not only depend on the intrinsic quality factor $Q_{int}$ of the disks but also on the coupling factor $Q_c$ that depicts the effective overlap between the bus WG mode and the WGMs and $Q_{split}$ that originates from the eventual splitting between clockwise (cw) and counterclockwise (ccw) propagating modes whose degeneracy is lifted due to surface imperfections [28, 41]. Beyond the critical coupling regime, $Q_{load}$ is seen to increase with increasing gap distance, $d_{gap}$, between the bus WG and the microdisk due to the exponential increase of $Q_c$. It is done at the expense of the transmission, which corresponds to the undercoupled regime [38]. Supplementary fabrication challenges occur when such a side-coupling scheme is implemented at short wavelengths due to the simultaneous need for (i) sub-100 nm $d_{gap}$ values to reach the critical coupling regime, (ii) etching of the upper part of the bus WG to avoid reabsorption phenomena occurring in the embedded active medium (cf. Figure 2), and (iii) the implementation of a bent bus WG to ensure optimum coupling between the resonator and the WG via an increase of the interaction length that also requires proper tuning of the WG width and the disk radius ($R$) [25].

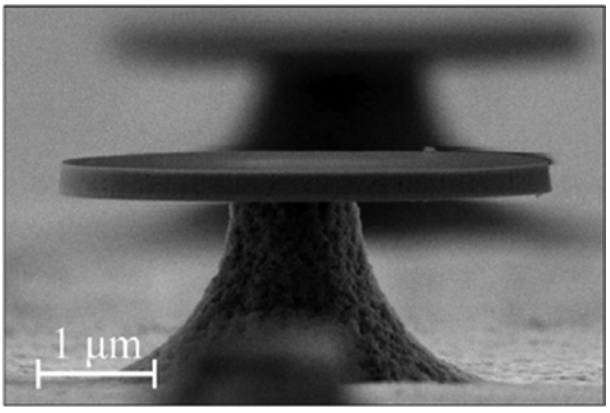


**Figure 3:** SEM profile of 4.0 μm diameter GaN disks with 1.2 μm diameter Si posts.
Reprinted from Ref. [37].

Let us briefly note that, beyond the above-mentioned circular microdisk fabrication schemes, more exotic approaches relying on selective area growth on *m*-plane GaN substrates [42] and lateral overgrowth on ZnO nanowalls grown on patterned graphene films [43] of hexagonal microdisks supporting both WGMs and quasi-WGMs have also been reported.

Finally, the readers more specifically interested in fabrication-related issues pertaining to III-N microdisks shall find more detailed explanations about this topic in two recent review articles: one by Zhang et al. [44] that covers all the disk geometries considered to date and a second one by Ren et al. [45] that focuses on PEC etched microdisk resonators and the role of defects such as unetched whiskers.

## 2.2 1D and 2D PhC membrane cavities

At first sight, the different processing steps described for the fabrication of III-N microdisks can be directly transposed to PhC membrane nanocavities. Historically, the first successful realization of such a structure, a point-defect L7-type GaN PhC slab nanocavity (Figure 4) with resonance modes close to 480 nm, was reported by the group of Evelyn L. Hu within the year after their report of mushroom-type GaN microdisks [17]. However, the fabrication task of small footprint PhC nanocavities poses extra challenges owing to the reduced feature size of the constitutive elements of the triangular PhC lattice, namely the lattice constant $a$ and the hole radius $r$. Indeed, in addition to the introduction of openings near the PhC pattern to ensure proper etching of either the sacrificial layer or the substrate, the etching conditions with the ICP-RIE have to be properly optimized to achieve air holes with smooth and vertical sidewalls in epilayers characterized by a high aspect ratio between the epilayer thickness and the hole diameter (height/width up to ~5). In particular, the need to have sub-100 nm diameter holes in the near-UV-visible range [18] leads to slower etch rates stemming from aspect ratio etching phenomena, namely a slowdown of the transport of reactive ions to the etched surface and neutral byproducts away from the etched surface that is hindered by gas-phase collisions, surface scattering, and surface charging [46]. In practice, the increase in the etch time to obtain a full etching of the holes through the III-N epilayers can lead to an overetching of the external dimensions, in particular for structures grown on Si (111) substrates, and requires the use of a thicker resist/hard mask [18]. This explains why early demonstrations of III-N PhC slab nanocavities were accompanied with a strong deviation of the sidewalls from the vertical and $Q$ values of <1000 [17].

Let us note that, compared to III-N microdisks, a wider variety of fabrication approaches have been reported for III-N PhC slabs. Thus, AlN epilayer structures grown on

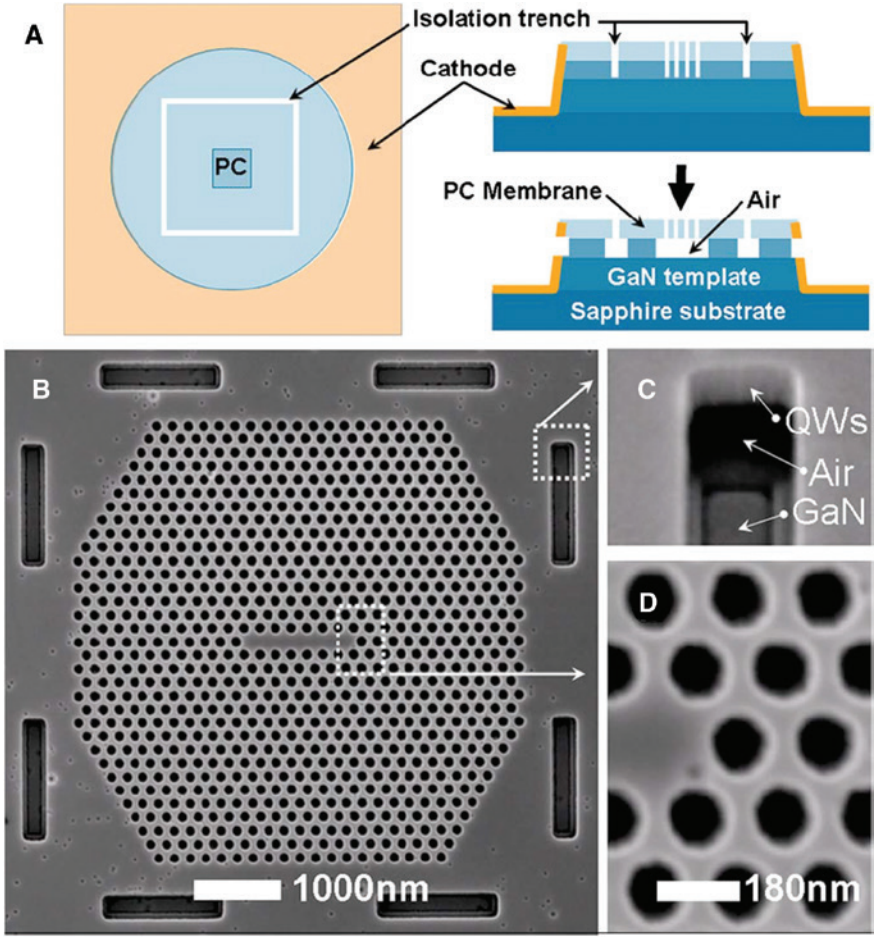


**Figure 4:** Fabrication details of an L7 GaN PhC membrane cavity.
(A) Schematic of PEC etching process to make PhC membrane nanocavities. (B) SEM image of an L7 cavity with lattice constant $a = 180$ nm and air hole radius $r \approx 60$ nm. (C) Side view of the rectangular opening. (D) Enlarged view of air holes near the center. Reprinted with permission from Ref. [17]. Copyright (2005) AIP Publishing.

6H-SiC (0001) substrates that benefit from a lower TDD than epilayers grown on both *c*-plane sapphire and Si substrates have been considered, but early attempts to release the membranes by PEC etching led to bent slabs and a degradation of the N-polar bottom AlN slab interface [19], hence explaining why it was later chosen to switch to a layer transfer technique to Si substrates using HSQ as a bonding layer and selective back-etching of the SiC substrate [47]. Such structures are often characterized by hexagonal air holes resulting from crystallographic orientation-dependent chemical reactions occurring during the PEC and ICP-RIE steps despite the use of circular hole patterns [19]. At one occasion, a bottom-up approach relying on the pre-patterning by EBL of an Si (111) substrate followed by conformal MBE growth of the III-N epilayer replicating the desired PhC pattern was also reported [48]. Thanks to their more resilient nature against structural and nonradiative defects, passive WG structures intended for NIR operation can be synthesized using low-cost nonepitaxial techniques such as sputtering. Thus, Pernice et al. have fabricated low footprint 1D AlN PhC nanobeam cavities, with $Q$ values up to 146,000, using sputtered-deposited AlN-on-insulator layers with a final sidewall residual surface roughness of <4 nm after wet etching of the underlying buried SiO layer with a buffered oxide etchant [49]. Such AlN nanobeams, whose cavity mode is centered in the C-band, were part of a PIC and could therefore be further characterized by means of a bus WG whose coupling gap was varied in the 200–700 nm range, hence allowing to switch from the overcoupled to the undercoupled regime. Another promising approach for the realization of *c*-axis-oriented membranes has been reported by Arita et al. The latter relies on the growth of an AlGaN WG layer lying on top of a sacrificial GaN-on-sapphire layer [50]. Test L7 AlGaN PhC slab nanocavities with an embedded InGaN QW medium were successfully obtained after the selective thermal decomposition of the GaN UL at ~1000°C under $NH_3/H_2$ ambient conditions that let $Al_xGa_{1-x}N$ epilayers nearly untouched compared to GaN for $x \geq 0.1$ (Figure 5). Finally, the fabrication of 1D and 2D PhC nanocavities from nonpolar zinc-blende AlN epilayers grown on 3C-SiC (001) pseudo-substrates has also been reported recently [51, 52].

Beyond the above-mentioned aspects, it is worth recalling that, for such defect-type 2D dielectric PhC slab cavities, which exhibit the smallest $V_m$ [53, 54] among 2D dielectric slab nanophotonic cavity structures – with the lowest value corresponding to the H0 cavity design [55], it was first empirically noticed by Akahane et al. [56] that an appropriate shift of air holes nearby the defect cavity leads to a gentle electric field confinement that is accompanied by a dramatic increase in the measured $Q$ values. It was later shown that, by taking advantage of increasing computing capabilities, an automated optimization scheme of PhC slab point-defect cavities based on a genetic algorithm accounting for both bulk absorption and fabrication disorder realizations enabled an exhaustive exploration of the parameter space to find a global maximum of the $Q$ and/or $\frac{Q}{V_m}$ value for a given material-cavity design combination [57]. Such an approach relies on the use of a small set of variational parameters, most often the spatial shift of a few holes next to the defect, and a Gaussian disorder model with zero mean and standard deviation $\sigma$. This type of approach was first successfully tested on small footprint Si (001) PhC membrane nanocavities exhibiting extremely high $\frac{Q}{V_m}$ values [58, 59], with an experimental $Q$ value ($Q_{exp}$) close to $2\times10^6$ being reported in an L3-type cavity [58] and low threshold power optical bistability in a H0 cavity [59], whose cavity mode wavelength was centered in the C-band and L-band, respectively. To verify the suitability of such an automated process based on a genetic algorithm in the framework of III-Ns, GaN PhC slab nanocavities of the L3-type design were computationally optimized and fabricated using lithographic tuning. More precisely, 20 groups ($g_{i=1-20}$) of cavities were processed, each one of them differing by a 1 nm step in the nominal hole radius, to account for uncertainty in the etching process [60]. Let us point out that with III-Ns, two sets of variational parameters were necessary for the global design optimization instead of only one in the case of Si PhC nanocavities due to the significantly lower refractive index contrast between this dielectric system and surrounding air. Thus, in addition to the outward shift of the three holes seating next to the defect cavity in the Γ-K direction of the triangular lattice, their radius was also part of the optimization scheme, which led to

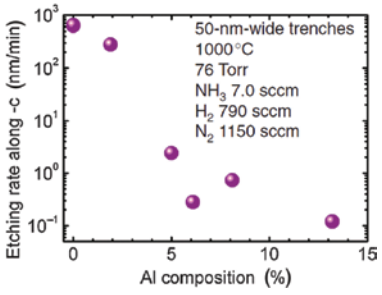


**Figure 5:** Al composition dependence of the thermal decomposition rate of the AlGaN alloy along the -*c* [000$\bar{1}$] direction. The annealing conditions used are listed in the figure. Reprinted from Ref. [50]. Copyright (2012) The Japan Society of Applied Physics.

their shrinkage compared to the remaining holes of the lattice. Beyond the very high average unloaded $Q$ value of 16,900 measured by means of the resonant light scattering technique in these modified L3 nanocavities at the resonant wavelength $\lambda \sim 1.3$ µm and a maximum experimental $Q$ value of 22,500, the important outcomes of this approach can essentially be summarized as follows. First, the quantitative agreement between values predicted by first principles simulations, where 100 disorder realizations were simulated for each group $g_i$, and the experimental statistics for both the $Q$ values and the resonant wavelength indicates the effectiveness and the consistency of this optimization method to improve PhC slab nanocavity designs for a given material family. Second, the fact that each group $g_i$ is characterized by experimental unloaded $Q$ values in excess of 10,000 highlights the technological maturity gained by small footprint III-N PhC slab nanocavities during the past few years. Such a statement is not only valid for NIR nanocavities but can also be transposed to shorter wavelengths. Indeed, the impact of fabrication disorder was successfully accounted for in the framework of 1D III-N PhC nanobeam cavities designed for the blue spectral range where the use of a single-step pattern transfer process allowed designing structures for which the standard deviation in the hole positioning and the hole diameter was reduced to 1 nm (Figure 6), i.e. a $\sigma$ value that matches the technical capabilities of the employed EBL tool [18]. Furthermore, such a progress in the fabrication was accompanied by a high yield of 97%, which was derived from the optical characterization of hundreds of nanocavity structures. Let us note that the quantitative estimate of the various parameters that govern the experimental $Q$ values of III-N microresonators and nanoresonators is precisely the subject of the first part of the next section of this review.

# 3 Optical properties of III-N microresonators and nanoresonators

## 3.1 Linear optical properties: a preliminary testbed for small footprint resonators

At first sight, one could consider that exploring the linear optical properties of III-N microresonators and

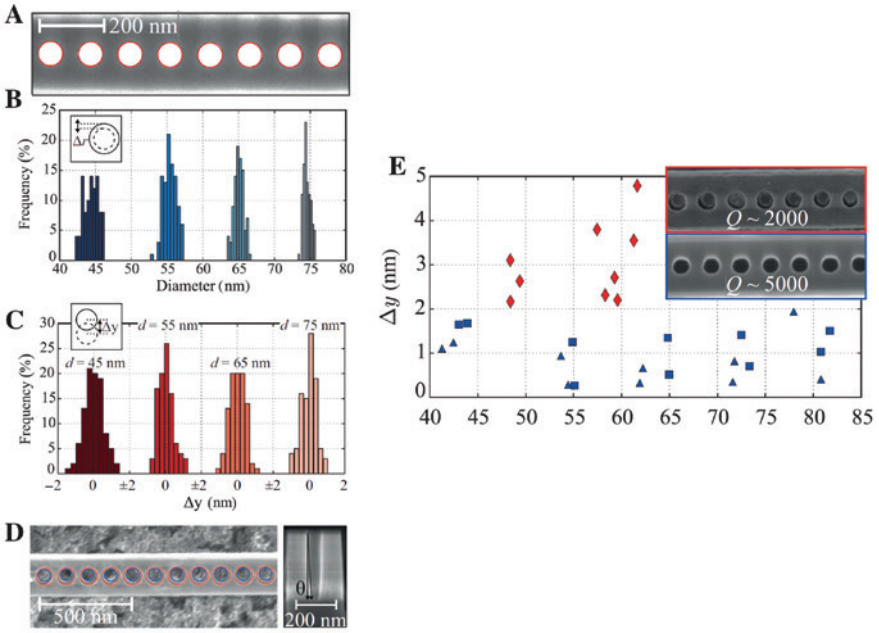


**Figure 6:** Critical dimension (hole size and position distribution) extraction from SEM images for modeling of fabrication disorder. (A) High-magnification view of nanobeam holes with algorithmically detected hole (white solid) and best-fit hole profile (red line). (B) Histogram of extracted hole diameters exhibiting Gaussian distributions with standard deviation of <1 nm. $N = 85$, 128, 158, and 60 holes were analyzed for the four target diameters, 45, 55, 65, and 75 nm, respectively. (C) Histogram of extracted hole centroid distances from the hole center line. (D) Hole sidewall deviation of $2.0 \pm 0.3°$ deduced from top views with critical dimension extraction (left) and cross-sections of cleaved etch test samples (right). (E) Positioning error $\Delta y$ for holes fabricated using a two-step mask transfer process (red diamonds) and the one-step mask transfer process pursued in this work (blue) for 200 nm (triangles) and 230 nm (squares) wide nanobeams. Insets show typical SEM images and average $Q$ factors. Adapted with permission from Ref. [18]. Copyright (2017) American Physical Society.

nanoresonators as a function of their operating wavelength is a pure tale of photonic disorder. Indeed, for resonators whose $Q_{exp}$ values stand far from the theoretical ones ($Q_{th}$), the observed decrease in the $Q_{exp}$ values with decreasing wavelength such as that reported in Figure 1 for III-N PhC slab nanocavities, which span a broad spectral range, is commonly ascribed to the increasing weight of Rayleigh scattering originating from fabrication-induced surface roughness. Within this framework, scattering losses are expected to lead to an overall decrease in $Q_{exp}$ that scales as $Q_{exp} \propto \lambda^3$ [28, 61], which is qualitatively verified by III-N PhC slab nanoresonators. However, we shall see that the precise determination of $Q_{exp}$ for a given resonator design by theoretical means is more complex than it may seem.

Before unveiling the dominant contributions governing $Q_{exp}$, let us point out that a proper, i.e. unambiguous, cavity mode identification should be carried out first. Obviously, this task is very much different depending whether we consider microdisks or PhC slab nanocavities. In the former case, we deal with a multimode device where, in the best-case scenario, the free spectral range (FSR) between two successive WGMs of the same radial number is simply given by $\frac{\lambda^2}{2\pi n_{eff} R}$ in the limit of large azimuthal mode numbers. With III-N microdisks, such a situation can be met provided the slab WG thickness only sustains the most fundamental TE/TM vertical modes, i.e. $m = 0$, and the post + disk diameters limit the number of radial mode families to <3. Due to the WG geometry, TE and TM modes will exhibit a dominant in-plane far-field radiation mode pattern with a stronger coupling to the far-field for TE modes [28, 62]. In addition, we already mentioned that surface imperfections such as surface roughness usually lead to a lift of the degeneracy between cw and ccw propagating modes [28, 41]. For short-wavelength operating III-N microdisk resonators with an embedded active medium, it is worth mentioning that experimentally a uniform distribution of WGMs across the entire spontaneous emission spectrum was only observed when using QDs rather than QWs [62]. This type of feature was originally ascribed to light reabsorption occurring at higher energy by InGaN/GaN QW states. This is a direct manifestation of the Stokes shift at play in these quantum heterostructures [29, 32]. A successful illustration of WGM identification was reported by Mexis et al. [62] using edge microphotoluminescence (μPL) collection from 2-μm-diameter thin *c*-plane AlN microdisk slabs with embedded GaN QDs emitting in the blue spectral range (Figure 7), i.e. a region where the oscillator strength of those big dots, as per III-N standards, is strongly reduced by the large built-in

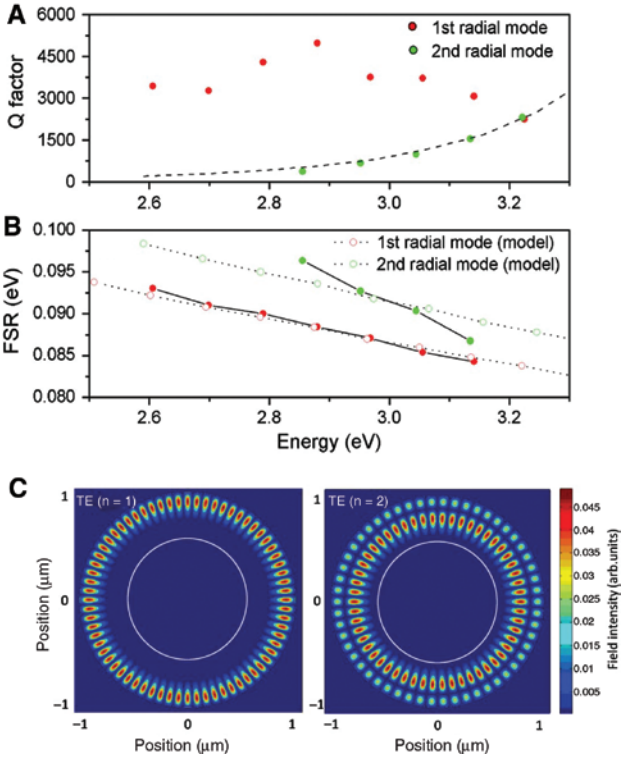


**Figure 7:** Measured WGMs and simulated optical modes of an AlN microdisk with four embedded GaN QD layers.
(A) *Q* values of the first and the second radial order families of WGMs for a ~2 μm microdisk. The dashed line is proportional to the inverse of the overlap of the second radial mode with the post that limits their *Q* factor. (B) FSR of the two mode families (full circles). Theoretical values are shown in open circles. (C) Example of simulated first (left) and second (right) radial order modes for a 2.06 μm diameter microdisk showing the TE field distribution within the disk plane (the light gray open circle represents the microdisk post periphery). Reprinted with permission from Ref. [62]. Copyright (2011) The Optical Society.

electric field that separates electron and hole wave functions. Hence, it makes this platform practically immune to the above-mentioned reabsorption phenomenon [32, 63]. $Q_{exp}$ values up to ~7300 were reported in such microdisk samples [62]. However, as can be understood, such an analysis cannot necessarily be easily performed in samples with slightly different parameters. Thus, it was verified with a set of nominally identical 3-μm-diameter GaN microdisks with a single InGaN/GaN QW medium characterized in the backscattering μPL geometry that exhibit $Q_{exp}$ values of several thousands [37]. In this latter case, the reason why no conclusive correspondence could be reached between 3D finite-difference time-domain (3D-FDTD) calculations and collected μPL spectra is due to the large number of parameters impacting the simulations, namely the large WG thickness $\left(\sim 3\frac{\lambda}{n_{eff}}\right)$ leading to multiple vertical nodes and the likely resulting mixture

of optical modes without any clear polarization dependence in the backscattered emission spectra, the extreme sensitivity of simulated spectra to the Si post diameter whose large complex refractive index in the blue spectral range leads to strong perturbations of higher order radial modes and lower order azimuthal modes due to their large electric field overlap with the post [37]. Furthermore, the release of the tensile strain at the free microdisk edges leading to a slight upward WG bowing (≤20 nm), as deduced from confocal micro-Raman spectroscopy and finite element simulations, and the Si post asymmetry resulting from the fabrication process were also seen to alter the simulated spectra [64]. Hence, in the vast majority of cases, such a complex combination renders any quantitative identification of WGMs in III-N microdisks rather elusive.

Conversely, despite their much larger design complexity compared to their microdisk counterparts, small footprint PhC membrane nanocavities sustain a much smaller number of cavity modes whose identification does not suffer from any such ambiguity. This is well documented in both the NIR and the visible spectral range (see, e.g. Refs. [34, 65] and Ref. [18], respectively). In particular, a very good agreement was reported between 3D-FDTD simulations of the optical modes and the vectorial mapping of the local density of states in GaN-based modified L3 PhC nanocavities through Fano imaging [66] performed using a scanning near-field optical microscope (SNOM), which offers deep subwavelength spatial resolution $\left(\frac{\lambda}{15} \sim 90\ \text{nm}\right)$ (Figure 8) [65].

Based on a previous analysis, to have a fully quantitative determination of $Q_{exp}$ in PhC slab nanocavities, the latter has to be be decomposed by considering up to six contributions depending on whether we are dealing with a passive or an active resonator. Thus, we get

$$Q_{exp}^{-1} = Q_{th}^{-1} + Q_{bk}^{-1} + Q_{gm}^{-1} + Q_{fab}^{-1} + Q_{ss}^{-1} + Q_{sa}^{-1}, \quad (1)$$

where $Q_{th}$ is related to pure radiation losses such as predicted by 3D-FDTD simulations for an otherwise perfect lossless structure, $Q_{bk}$ corresponds to bulk absorption losses, $Q_{gm}$ corresponds to the optical losses originating from the eventual presence of a gain medium (QWs or QDs), $Q_{fab}$ corresponds to the optical losses induced by fabrication disorder, $Q_{ss}$ corresponds to the optical losses due to surface scattering, and finally $Q_{sa}$ accounts for surface absorption-related optical losses.

As far as the determination of $Q_{th}$ is concerned, the guided-mode expansion (GME) method [67], which was benchmarked against 3D-FDTD simulations, used to be the technique of choice to determine the theoretical $Q$ of a particular design thanks to its fast computational time. GME was combined to the genetic algorithm of the Matlab Global Optimization Toolbox to derive the global maximum when considering the set of relevant variational parameters for a given material platform [57, 58]. However, later reports

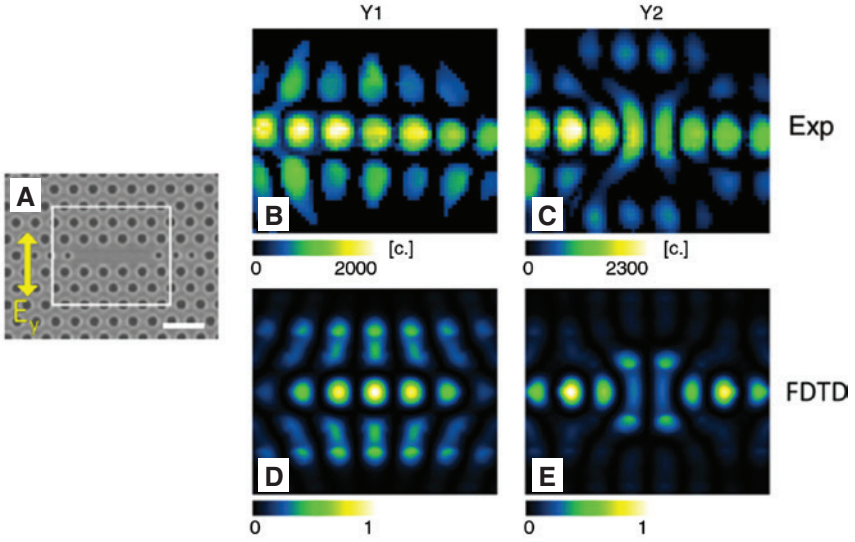


**Figure 8:** Resonant forward scattering (RFS) data and FDTD simulations of Y1 and Y2 modes in the *y* polarization channel.
(A) SEM image of the GaN L3 PhC nanocavity sample where the white rectangle shows the area scanned in the SNOM measurements. Scale bar, 1 μm. (B and C) Experimental maps of the Fano amplitude measured in RFS configuration for Y1 and Y2 modes, respectively. (D and E) FDTD calculations of $|E_y|^2$ for Y1 and Y2 modes, respectively. FDTD maps are normalized to their maximum value. All the maps correspond to a 3.0 × 2.5 μm area. Reprinted with permission from Ref. [65]. Copyright (2015) AIP Publishing.

mostly relied directly on 3D-FDTD simulations thanks to the large increase in computational capabilities [18, 31, 60]. In any case, the computed $Q_{th}$ values for III-N PhC membrane nanocavities always outperform experimental values [12, 13, 18, 47, 68–71] even in the case of high-$Q$ NIR 1D-PhC AlN nanobeam cavities (Figure 9) [49], so that its weight is often discarded when evaluating $Q_{exp}$.

Hence, one of the next contributors to be considered as a major source of loss is bulk absorption loss, whose expression is given by the common relationship $Q_{bk} = \frac{2\pi n_{eff}}{\lambda\alpha}$ [72], where $\alpha$ corresponds to the residual absorption coefficient in the WG. Let us note that, in the previous expression, we can explicitly discard the optical losses induced by the gain medium, $Q_{gm}$, if present. Indeed, the contribution of the latter can be canceled by pumping the PhC membrane or the microdisk near transparency. From there, the internal modal loss occurring in the III-N WG epilayer of interest can be estimated from net modal gain measurements performed with the variable stripe length method before any processing step [18, 73].

As mentioned above, it has been shown that $Q_{fab}$ can be reliably estimated by relying on a genetic algorithm accounting for fabrication disorder by considering a Gaussian disorder model whose mean and standard deviation are derived from experimental observations [18, 57–60]. A thorough quantitative statistical analysis of the impact of fabrication disorder pertaining to short-wavelength III-N PhC nanocavities can be found in the work of Rousseau et al. [18]. At this stage, we can point out that $Q_{exp}$ values have been successfully accounted for at NIR wavelengths when dealing with a statistical set of lithographically tuned small footprint GaN PhC slab nanocavities on the sole basis of absorption losses and fabrication disorder (Figure 10), i.e. $Q_{exp}^{-1} = Q_{bk}^{-1} + Q_{fab}^{-1}$, where a $\sigma$ value of 5 nm was considered for modeling disorder due to the use of a two-step pattern transfer process, the contribution of $Q_{th}$ being indeed negligible [60]. In this latter case, quantitative agreement between simulations and experimental results was obtained for a $Q_{bk}$

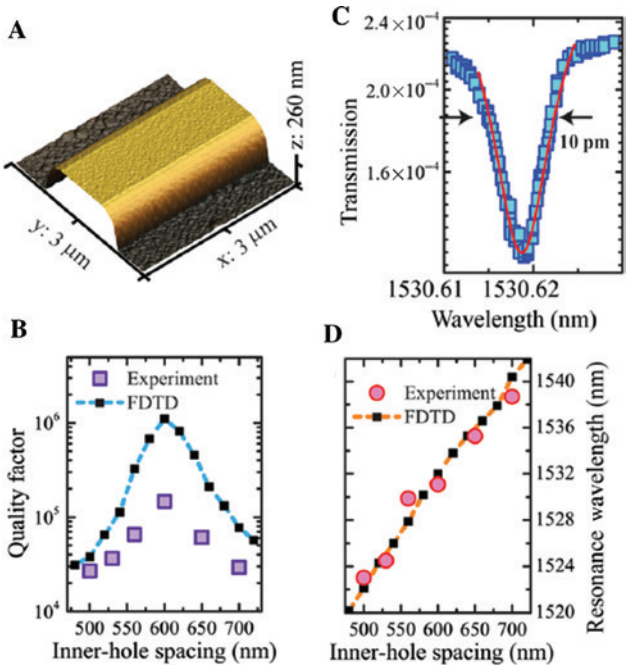


**Figure 9:** Properties of a 1D AlN PhC nanobeam cavity designed for NIR operation.
(A) AFM image of the WG profile showing top surface rms roughness of 1.2 nm after fabrication and 3.5 nm sidewall roughness. (B) Tuning of the cavity resonance in dependence of the inner-hole spacing. The best optical $Q$ of 146,000 is found for an inner-hole spacing of 600 nm. (C) Detailed spectrum of the cavity resonance with highest $Q$ factor of 146,000. (D) Resonance wavelength increases with inner-hole spacing. A length change from 500 to 700 nm shifts the resonance wavelength by 15 nm. Reprinted with permission from Ref. [49]. Copyright (2012) AIP Publishing.

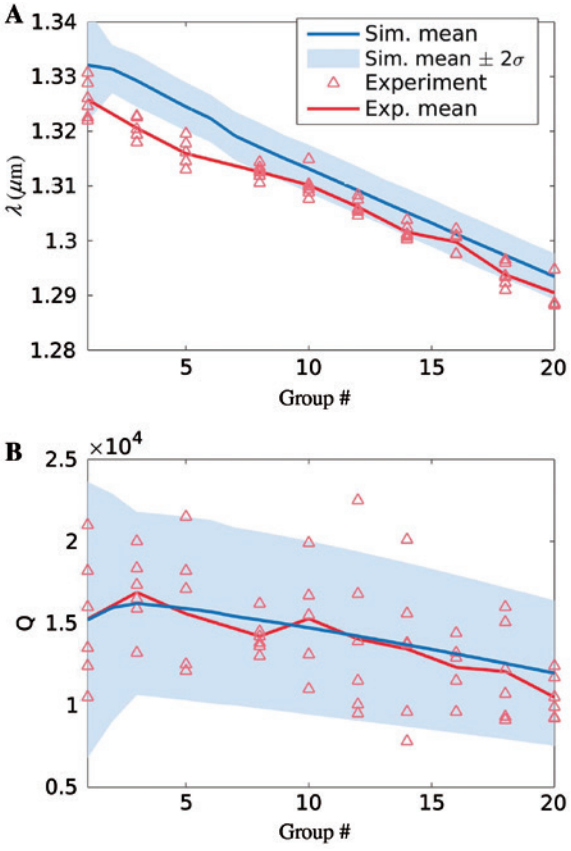


**Figure 10:** Experimental and simulated optical properties of modified L3 GaN PhC cavities designed for the NIR spectral range.
(A) Resonance wavelengths and (B) quality factors as a function of the cavity group number $g_i$. The red (blue) color refers to experimental (simulated) data. Reprinted with permission from Ref. [60]. Copyright (2014) AIP Publishing.

value of 40,000 corresponding to a residual absorption coefficient of 2.8 $cm^{-1}$ at $\lambda \sim 1.31$ μm using $n_{eff} = 2.33$. It is fully consistent with the value of 1.8 $cm^{-1}$ at $\lambda = 1575$ nm deduced from power-dependent cavity in-plane transmission measurements done on width-modulated GaN WG cavities by Roland et al. [69]. The potential impact of surface scattering, i.e. losses other than those introduced by fabrication disorder, and that of surface absorption at NIR wavelengths in small footprint III-N PhC nanocavities remains to be shown. We can, however, emphasize that, for suspended III-N PICs and long 1D PhC WGs, scattering losses due to the presence of tethers are a well-established experimental fact that requires an aperiodic positioning of the latter to minimize Bragg resonances and hence transmission losses [24, 69, 74, 75].

One could reasonably argue that probing the signature of both $Q_{ss}$ and $Q_{sa}$ in III-N microresonators and nanoresonators appears as devoid of any sense based on the usual assumptions regarding fabrication-related issues with this material family (see, e.g. Ref. [45]). However, the recent use of a single-step pattern transfer process leading to an EBL resolution-limited $\sigma$ value of 1 nm, which has only been reported at visible wavelengths with 1D GaN PhC nanobeam cavities thus far [18, 37], enabled a sample fabrication quality with $Q_{exp}$ values requiring the determination of the respective weight of these two quantities. This feature was restricted up until now to Si- and GaAs-based microdisks [28, 76] and Si-based PhC membrane nanocavities [77]. Thus, $Q_{ss}$ values can be precisely estimated by first extracting the top and bottom surface roughness and waviness of membranes from multiscale atomic force microscopy (AFM) measurements [37]. Such mappings can then serve as inputs to generate the 2D autocorrelation function of height values that leads to the power spectral density function of surface roughness in $k$-space via the Wiener-Khinchin theorem [78]. The next step consists of generating algorithmically rough and wavy surfaces [79] that serve as input parameters for electromagnetic computations that rely on the volume current method [80], from which $Q_{ss} = \frac{2\pi c}{\lambda}\frac{U}{P_{ss}}$ is deduced [28, 81], where $U$ is the amount of energy stored in the resonator and $P_{ss}$ is the power due to surface scattering radiated through a half-sphere enclosing the PhC that is computed along the lines given in Ref. [81]. It appears that the scattering losses due to the surface waviness measured on GaN membranes representative of fabricated 1D GaN PhC nanobeam cavities lead to $Q_{ss}$ values one to two orders of magnitude larger than those experimentally measured (Figure 11) [18, 64]. It is explained by the much smaller overlap of the simulated electric field intensities with the top and bottom surfaces compared to the overlap with the vertical sidewalls whose impact is partially accounted for when computing $Q_{fab}$ [64]. Achieving a precise, and hence quantitative, estimate of the vertical sidewall roughness, in particular inside etched holes, is an experimental challenge in itself. Nonetheless, SEM measurements provide an upper bound on the sidewall root mean square (rms) roughness to a value of ~2 nm, whose impact leads to computed $Q_{ss}$ values for this sole contribution on the order of $Q_{th}$. It explains why its contribution can be safely neglected.

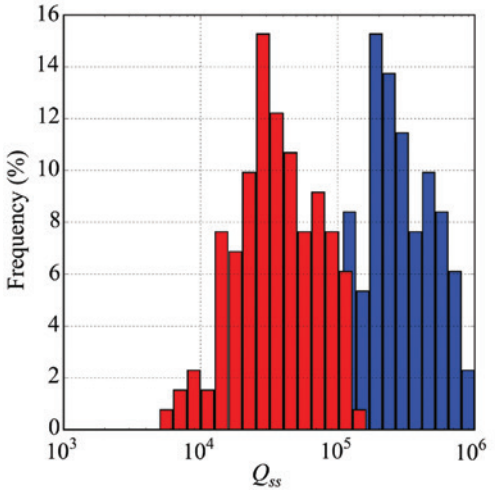


**Figure 11:** Quality factor limited by scattering losses ($Q_{ss}$) due to a 4.9 nm rms surface waviness computed by the volume current method for the nanobeam geometry from Ref. [18]. Here, 131 realizations of surface waviness were simulated to construct the histograms of the fundamental longitudinally symmetric (blue) and first-order longitudinally antisymmetric (red) cavity modes supported by the nanobeams [64].

Based on our analysis of $Q_{exp}$ constituents, it appears that surface absorption should account for a significant fraction of the observed losses in the blue spectral range in state-of-the-art GaN PhC membrane nanocavities. Considering the high surface-to-volume ratio of these resonators and the fact that III-Ns exhibit deep, localized surface states within the bulk material bandgap, such a statement is not at odds with the reported observations. More precisely, it is well-known that, in $n$- and nonintentionally doped (*nid*) GaN epilayers, the Fermi level is pinned by a high density of intrinsic, unoccupied surface states below the conduction band minimum [82, 83]. It results in the formation of a space charge region and upward band bending at the GaN surface in thermal equilibrium. As far as optically active surface states of the most relevant planes are concerned, namely the +$c$- and $m$-plane GaN surfaces, unoccupied states exist in the range of 2.4–2.9 eV above the valence band maximum [84–86]. Thus,

preliminary measurements performed under continuous wave optical pumping at 351 nm in ambient atmosphere on 1D GaN PhC nanobeam cavities revealed an irreversible deposition occurring on the sample surface, whereas no such deposition was observed when similar experiment was done under vacuum [18]. To gain further insights into the potentially harmful role of optically active surface states on $Q_{exp}$ via $Q_{sa}$, photoinduced gas desorption experiments were carried out in a controlled atmosphere by monitoring the time-dependent evolution of μPL spectra of microdisks at room temperature (Figure 12A) [37], this latter type of structure having the advantage to exhibit a high number of optical modes. In particular, it was noticed that oxygen desorption induces a strong increase of optical attenuation by *m*-plane surface state absorption, knowing that the *m*-plane corresponds to the most critical orientation for the cavity modes supported by the III-N microresonators and nanoresonators under review. In a nutshell, upon oxygen desorption triggered by the photogenerated holes, the Fermi level on the surface gets unpinned, which modifies the surface charge and the width of the space charge region. WGMs redshift and broaden upon UV-induced photodesorption at 300 K with a rate that depends on the UV pump power. When introducing oxygen in the chamber, a near-complete recovery of the spectra is observed showing the reversibility of this process. All those WGM changes (spectral shift and broadening) that strongly rely on the vacuum pressure can be translated into effective changes in the refractive index [37, 77] and likely into changes in the surface absorption rate coefficient [28]. In GaN microdisks, changes in the absorption coefficient $\Delta\alpha$ up to 100 $cm^{-1}$, which are limited by the InGaN/GaN QW μPL background emission and which correspond to an upper $\Delta Q_{sa}$ value of ~3400 at 450 nm, could be measured [37]. Importantly enough, no qualitative change could be observed in the WGM redshift and broadening upon oxygen desorption between $n^+$-doped and *nid* GaN microdisk samples [37]. Finally, let us also note that the possible impact of sample heating could be ruled out through a study combining confocal micro-Raman spectroscopy measurements of the peak shift of the GaN $A_1$(LO) Raman mode as a function of laser power density and finite element modeling of heat transport in a GaN microdisk. Indeed, an elevation of 30°C at most above room temperature was predicted at the power density used for triggering UV photodesorption of oxygen [37]. It is well below the temperature where either oxygen desorption from GaN surfaces is expected to occur (950°C) [87] or water vapor may be converted to an oxide-like surface layer (200°C) [88].

The key role played by surface states and related surface absorption on the optical properties of III-N

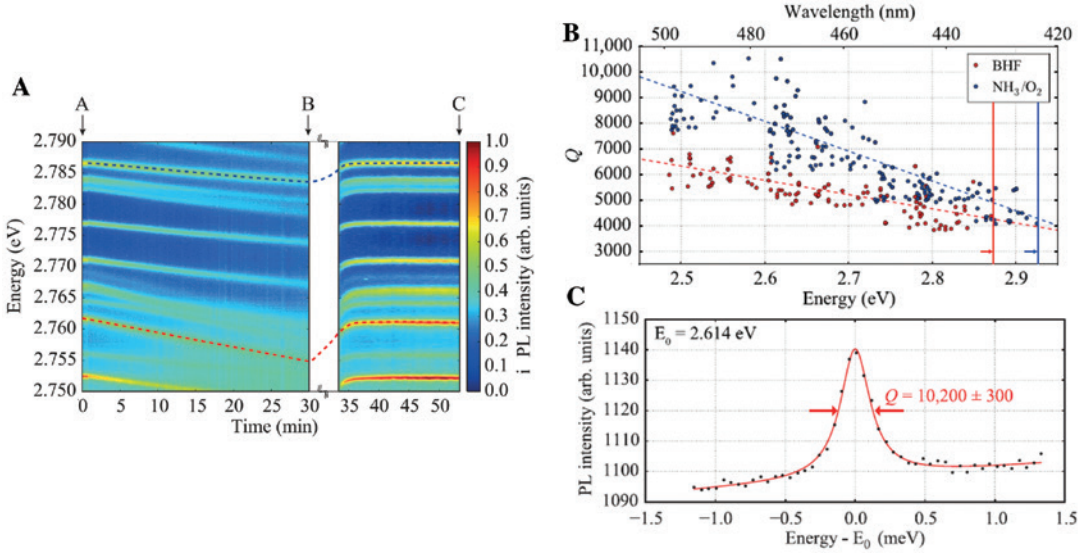


**Figure 12:** Optical properties of a mushroom-type GaN microdisk with a single InGaN QW.
(A) Nearly reversible redshift and broadening of microdisk resonances caused by photoinduced desorption and adsorption of oxygen from III-N surfaces at room temperature. Normalized PL time dependence under high vacuum (<$10^{-3}$ mbar) using optical pumping at 4.6 kW $cm^{-2}$ with a 325 nm cw laser shown with the QW PL background removed. At $t = 30$ min, $O_2$ is injected. (B and C) PL energy and surface treatment dependence of quality factor measured at 5 K under 325 nm cw optical pumping at 460 W $cm^{-2}$. In (B), two surface treatments are examined sequentially on the same sample, 49% buffered hydrofluoric acid (red) followed by annealing in $NH_3$ and $O_2$ at 750°C (blue). Dashed lines are linear regressions and solid lines show the energy cutoff. (C) μPL signal and Lorentzian fit for a high-*Q* mode at ~2.6 eV. The spectrometer resolution corresponds to a *Q* of 14 000. Adapted from Ref. [37].

microresonators and nanoresonators obviously calls for remedies. Hence, preliminary surface passivation solutions were investigated through both surface treatments and thin-film coatings. Regarding surface treatments, among the various cleaning and passivation techniques that were explored, sample preparation in 49% buffered hydrofluoric acid solution followed by annealing in $NH_3$ and $O_2$ at 750°C led to low and high oxygen-content surface, respectively, and hence low and high $Q_{exp}$ values (Figure 12B) [37]. This allowed to measure for the first time $Q$ values in excess of 10,000 in the blue spectral range from small footprint III-N resonators (Figure 12C). In addition to the monotonous decrease in $Q_{exp}$ with decreasing wavelength that is likely originating from the increasing weigth of $Q_{bk}$, $Q_{fab}$, and $Q_{sa}$, a high-energy cutoff is observed for GaN microdisk near 2.9 eV (Figure 12B). It appears that such an energy value does coincide with the theoretically predicted peak in the joint density of optically active surface states for *m*-plane GaN [83, 85] and the pinning of the Fermi level above the valence band maximum measured on GaN nanowires [89]. This energy is larger than that measured on clean and stoichiometric nonpolar GaN($10\bar{1}0$) *m*-plane surfaces freshly cleaved in ultra-high vacuum [86]. It could stem from surface reconstruction and a change in surface chemistry due to nitrogen atom desorption taking place during the dry etching process, hence leading to nonstoichiometric sidewalls (e.g. by introducing nitrogen vacancies) [90, 91]. It is akin to what has been reported in Si microdisks after RIE damage [28]. In any case, the sensitivity of surface states and their impact on the optical features may likely be responsible for the observed blueshift by about 50 meV in the cutoff energy after optimized annealing treatment (Figure 12B, blue vs. red vertical solid lines).

Despite the critical importance of surface treatments, the latter did not lead to any stable, i.e. long-term, protective chemisorption solution thus far. Therefore, the encapsulation provided by a thin-film coating could seem a much better suited approach as *a priori* we could expect a complete protection of the resonators from their surrounding environment, e.g. by passivating surface states, without introducing any additional losses due to absorption or scattering. However, to reach such a goal, a conformal coating technique is desired to ensure the proper coating of the sidewalls, among which those of tiny holes ($r < 50$ nm) of PhCs, as well as the undersides of the suspended membranes. Although atomic layer deposition (ALD) is known for its conformal character, low-temperature deposition from organometallic precursors does likely result in a nonnegligible carbon incorporation into the thin films [92]. It would explain the significant $Q_{exp}$ degradation even after subsequent annealing of the ALD-coated resonators (attempts included both $HfO_2$ and $Al_2O_3$) in ammonia and oxygen at 750°C. The exact nature of the observed additional losses remains unclear and could be due to either absorption induced by impurities present in the ALD-deposited layer or changes in the GaN surface occurring upon ALD deposition. Attempts based on the PECVD of $SiO_2$ indicate that this technique is suitable for conformally coating the underside of mushroom-type III-N microdisks but not the interior surface of PhC holes (see Supplementary Material section 1). Thus, $SiO_2$-coated 3-μm-diameter GaN microdisks annealed in ammonia and oxygen for 5′ each exhibit similar maximal $Q_{exp}$ values to uncoated microdisks that have experienced the same optimized surface treatment, thereby indicating that this approach does not introduce any additional scattering losses and that the postcoating annealing treatment is amenable to cure surface absorption occurring at the nitride-$SiO_2$ interface (Supplementary Material Section 1).

Let us emphasize that this extreme sensitivity of III-N resonators to surface effects has already been exploited in a few occasions for different purposes. Thus, Aharonovich et al. reported on the controlled WGM tuning by immersing microdisks in deionized water and performing UV laser irradiation [93]. Using controlled tuning rate, permanent, i.e. irreversible, wavelength tuning with an accuracy on the order of 1 nm was reported at low excitation power, without degrading optical features, which was ascribed to selective *in situ* oxidation of the studied InGaN/GaN microdisks. Those authors demonstrated later that WGM tuning could reach the equivalent of one FSR and that the mode wavelength tuning rate was linear vs. power density (for a fixed time duration) and time (for a fixed power density) [94]. It was argued as being a promising step toward tailored CQED approaches. Similarly, Kouno et al. showed that high filling factor patterned hexagonal AlGaN microdisk arrays dipped into different solutions could offer an interesting potential for microsensing and 2D microimaging applications through real-time monitoring of the room temperature shift of the PL of WGMs [95]. In addition to these two surface effect signatures reported in liquid solutions, the above-mentioned UV-photoinduced oxygen adsorption and desorption phenomena hint toward the gas sensing potential of small footprint air-clad III-N resonators. In this regard, preliminary experiments carried out on 1D GaN PhC nanobeam cavities indicate the large tuning of fundamental and first-order PhC cavity modes by photoinduced gas adsorption using UV illumination at room temperature (Supplementary Material Section 2). In particular, gases such as $O_2$, $N_2$, $CO_2$, or He exhibit a unique gas tuning curve, which is ascribed to the selectivity of

surface states to the chemical species that leads to specific changes in surface absorption. A relative tuning range $\frac{\Delta\lambda}{\lambda}$ on the order of a few percent has been recorded, which exceeds by far the values of $>10^{-3}$ reported in air-slot PhC nanocavities [96].

To conclude this subsection, we summarize the main features related to the fabrication and the optical properties of the state-of-the-art III-N photonic cavities listed in this review in Table 1.

## 3.2 Optical nonlinearities of NIR resonators

Contrary to their linear optical properties and, as we shall see, the demonstration of lasing features, studies focusing on the nonlinear optical properties of small footprint air-clad III-N microresonators and nanoresonators remain relatively scarce and have been mostly reported by the group of Philippe Boucaud et al. using both the microdisk and the PhC platforms [38, 39, 100, 101]. As pointed out by Jung et al. [6, 102], beyond the basic features enumerated in the introduction, the ability to fabricate high-quality optical resonators made from GaN or AlN that exhibit both second-order Pockels [$\chi^{(2)}$] and third-order Kerr [$\chi^{(3)}$] optical nonlinearities is likely to spark additional interest in this material family for implementing novel optical devices spanning a wide range of wavelengths such as on-chip self-referenced optical frequency combs.

As far as air-clad microdisks are concerned, a first interesting outcome arising from continuous-wave resonant second harmonic generation (SHG) experiments deals with the observation of the mode pattern associated with the harmonic cw and ccw propagating modes originating from the above-mentioned surface imperfections. Indeed, the twice lower diffraction limit at $2\omega$ leads to an increased spatial resolution that allows for a precise spatial profile mapping of the NIR resonant modes at the angular frequency $\omega$ with, in particular, the clear discrimination between first- and second-order radial modes, which was further confirmed by a good agreement with FDTD calculations [38]. This was followed by phase-matched continuous-wave SHG occurring in doubly resonant on-chip GaN-on-Si microdisks [39]. Such phase matching was made possible through lithographic tuning of the microdisks, which allowed to design structures where fundamental and second harmonic waves are matched with modes that fulfill the conservation of orbital momentum, i.e. $\Delta l = l_{SHG} - 2l_{pump} = 0$, where $2l$ is the number of antinodes in the azimuthal near-field profile. The moderate $Q_{load}$ value around 10,000 in the S- to L-telecommunication

**Table 1:** State-of-the-art III-N photonic cavities fabricated from epilayers grown on different substrates.

| Substrate type | TDD ($cm^{-2}$) | Crystal phase | Sacrificial layer type | WG type | Membrane release method | Cavity design | $\lambda$ (nm) | $Q_{max}$ | Ref. |
|---|---|---|---|---|---|---|---|---|---|
| *c*-plane sapphire | $0.7–2\times10^9$ | WZ | InGaN/InGaN SL | GaN | PEC etch | L7 | ~480 | 800 | [17] |
| *c*-plane sapphire | $0.7–2\times10^9$ | WZ | InGaN/InGaN SL | GaN | PEC etch | Microdisk | 476 | 6600 | [97] |
| *c*-plane sapphire | $0.7–2\times10^9$ | WZ | GaN | AlGaN | Thermal decomposition | L7 | 463 | 5100 | [50] |
| Nanopatterned Si (111) | Unspecified | WZ | Si (111) | AlN | HF/nitric acid/acetic acid | L3 | 425 | 1800 | [48] |
| Si (111) | $5\times10^{10}$ | WZ | Si (111) | GaN | $XeF_2$ | Microdisk | 474 | 10,200 | [37] |
| Si (111) | $5\times10^{10}$ | WZ | Si (111) | AlN | $XeF_2$ | Microdisk | 285 | 4400 | [30] |
| Si (111) | $5\times10^{10}$ | WZ | Si (111) | AlN | $XeF_2$ | Microdisk | 1584 | 80,000 loaded | [38] |
| Si (111) | $5\times10^{10}$ | WZ | Si (111) | GaN | $XeF_2$ | 1D nanobeam | 441 | 7950 | [64] |
| Si (111) | $5\times10^{10}$ | WZ | Si (111) | GaN | $XeF_2$ | H0/L3 | 1513/1545 | 44,000/41,000 | [70] |
| 6H-SiC | Unspecified | WZ | 6H-SiC | AlN | PEC etch | L7 | 383 | 2400 | [19] |
| 6H-SiC | Unspecified | WZ | 6H-SiC | AlN | Epilayer transfer and $SF_6$ ICP-RIE | Ladder nanobeam | 403 | 6900 | [98] |
| AlN-on-insulator | Unspecified | WZ | $SiO_2$ | AlN | Wet etch in buffered oxide | 1D nanobeam | 1531 | 146,000 | [49] |
| *m*-plane GaN | Unspecified | WZ | $In_{0.08}Ga_{0.92}N$ | GaN | PEC etch | Microdisk | ~420 | 2000 | [20] |
| C-SiC template on Si (001) | Unspecified | ZB | 3C-SiC template | AlN | $CF_4$ RIE | Microdisk | 311 | 5000 | [99] |
| C-SiC template on Si (001) | Unspecified | ZB | 3C-SiC template | AlN | $CF_4$ RIE | H1/L3 | 354/360 | 4400/5000 | [52] |

WZ, Wurtzite; ZB, zinc-blende.

bands has proven to be a good tradeoff between the interaction length provided by the straight in-plane WG-microdisk configuration and the bandwidth of frequency conversion. The strong enhancement of frequency conversion reported experimentally for those phase-matched microdisks was also satisfactorily reproduced by the coupled mode theory using the detuning between the NIR pump and the second harmonic as adjustable parameter, hence illustrating once more the suitability of lithographic tuning approaches [39]. Furthermore, let us note that, despite their lower nonlinear optical susceptibility compared to their GaAs counterpart ($\chi^{(2)}_{zzz} \sim 20$ pm/V [103] vs. 188 pm/V for $\chi^{(2)}_{xyz}$ [104]) and the necessity to optimize the coupling scheme between microdisks and WGs to improve the absolute conversion efficiency, high-$Q$ resonators with a high field strength made from AlGaN epilayers offer the advantage to be transparent in the visible and hence to be much less sensitive to undesired nonlinear effects such as optical bistability stemming from two-photon absorption, free-carrier absorption, and thermal instability that are at play, e.g. in the equivalent Si platform [59, 70].

When switching to III-N PhC membrane cavities, two main designs can be considered for SHG and third harmonic generation (THG) that essentially differ by their mode volume. On the one hand, Zeng et al. focused on so-called width-modulated WG cavities characterized by a $Q_{exp}$ value in excess of 15,000 in the C-band and L-band and a mode volume that is well above the diffraction limit [100, 101]. Such a geometry is well adapted for PICs, as the light is guided in the PhC by adopting a W0.98 WG design. Using a light collection scheme perpendicular to the PhC plane, those authors first reported a quadratic dependence of the integrated SHG signal as a function of incident power at the entrance of the PhC WG with a measured "threshold" input power of 70 μW using continuous-wave resonant excitation [100]. An additional signature of the SHG process stemmed from the narrower lineshape of the second harmonic signal, matching a squared Lorentzian fit, compared to the transmission resonance of the cavity [100]. High spatial resolution imaging of the second harmonic signal was found to be in good agreement with the near-field emission pattern calculated via 3D-FDTD simulations, including the proper susceptibility tensor components. The next step with this width-modulated WG cavity geometry was the report of THG in the green spectral range under continuous-wave resonant excitation using the same in-plane excitation perpendicular light collection/high-resolution imaging scheme as for SHG [101]. In the absence of any phase matching, i.e. without the intended design of a resonant cavity mode for the third harmonic signal, the THG power was seen to exhibit a cubic power law dependence on pumping power coupled to the cavity. It was accompanied by a THG signal whose spectral dependence matched the cubic power of the Lorentzian used to fit the fundamental mode. In a way similar to the previous SHG study, a good quantitative agreement was achieved between the measured high spatial resolution images of the polarization-resolved third harmonic radiated patterns and their 3D-FDTD simulated counterparts accounting for the relevant $\chi^{(3)}$ tensor components, namely when comparing the symmetry and the in-plane extension of the THG spots that exhibit a width of >300 nm. The reported $\sim\frac{\lambda}{5}$ spatial resolution is argued to be a strong asset of this imaging technique that would be a competitive alternative to the SNOM technique [65], owing to its ease of implementation, the absence of any perturbation of the near-field induced by a tip, and its suitability to even characterize nanophotonic structures with $Q_{exp}$ value in excess of 1 million [101]. On the other hand, Sabry Mohamed et al. have investigated small footprint high $\frac{Q}{V_m}$ ratio genetically optimized L3 and H0 GaN PhC cavities exhibiting $Q_{exp}$ values of 41,000 and 44,000 in the S-band and the C-band as deduced from the above-mentioned resonant light scattering technique, respectively [70]. A peculiar feature of these lithographically tuned samples lies in the optimization of their design for both mode coupling and confinement, each having a set of holes next to the cavity specifically engineered to act as injectors and allow for proper manipulation of out-of-plane radiative losses. This led to experimental coupling efficiencies at the fundamental angular frequency that lies between 3% and 19% for L3 cavities and 2% and 15% for H0 cavities, depending on the injector hole radius, in agreement with the targeted values. SHG was observed under resonant continuous-wave excitation as confirmed by the quadratic power dependence of the collected SHG signal upon increasing coupled power and the squared Lorentzian intensity lineshape of the SHG emission as a function of excitation wavelength. A lower bound value of $2.4\times10^{-3}$ W$^{-1}$ for the normalized SHG conversion efficiency was measured that compares favorably to values reported in GaN microdisk resonators [39] and larger footprint GaN ring resonators [105]. By adopting a doubly resonant scheme in such PhCs, an SHG conversion efficiency closer to that obtained with state-of-the-art AlN ring resonators is even expected [106]. THG in the green occurred simultaneously to SHG with a power law intensity ratio as a function of input power of 1.4 slightly below the expected 1.5 ratio (Figure 13). This study allowed to conclude that, despite its larger $V_m$ value, the L3 cavity

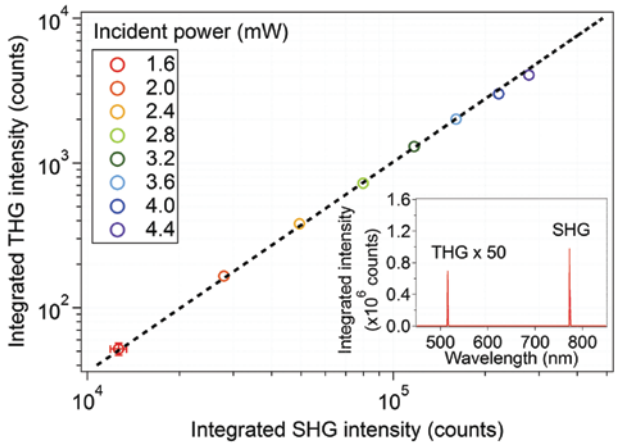


**Figure 13:** Plot of the collected SHG vs. THG intensity as a function of the power incident on an optimized L3 cavity under resonant excitation at $\lambda = 1545$ nm.
Inset, cavity's emission spectrum, displaying SHG and THG at a wavelength of 772.5 and 515 nm, respectively, with the latter scaled for visibility. Reprinted from Ref. [70].

design was better suited than the H0 one for SHG emission for structures with a comparable $Q_{exp}$ value due to the enhanced coupling factor of the former geometry originating from the better overlap between the Gaussian excitation beam and the orientation of the mode field components [70].

Finally, let us point out that all those results clearly illustrate the increasing degree of maturity gained by III-N microresonators and nanoresonators in the past 15 years, as acute nonlinear phenomena can be triggered and probed under continuous-wave resonant excitation while simultaneously allowing for high spatial resolution imaging, which is a fairly unique feature not accessible with the equivalent Si and III-As/III-P platforms.

## 3.3 Microlasing and nanolasing features in the UV to visible range

The observation of lasing features in dielectric optical resonators is a major landmark in the field of microphotonics and nanophotonics, as it is often considered as a way to validate the fabrication and the quality of such devices. Both the mushroom-type microdisk [26] and the PhC membrane cavity [107] geometries proved to be suitable to sustain lasing in small footprint dielectric systems. Similar features have been reported in the III-N material platform, although to date the demonstration of lasing in III-N PhC membrane nanocavities remains limited to the sole 1D PhC nanobeam geometry [12–14].

If one focuses first on microdisks, lasing has been initially reported by Haberer et al. in PEC-etched GaN microdisk structures using InGaN/GaN multiple QWs as gain medium under pulsed excitation that exhibits a reasonably high $Q_{exp}$ value of ~4600 at transparency [16]. The large peak power density required to get lasing did not allow for a systematic study of these devices in the stimulated emission regime. It was partly ascribed to the low thermal dissipation rate associated with the air-clad geometry and the subsequent degradation of the gain region as well as scattering losses due to the nonnegligible sidewall roughness. Another recognized potential drawback with the microdisk geometry originates from the small FSR between WGMs, which leads to mode competition over the gain band that typically covers an optical bandwidth between 10 and 20 nm in the blue spectral range [108] and hence an expected reduced β value in such devices. Nonetheless, the same group was the first to report lasing under room temperature continuous-wave optical pumping using a HeCd laser with a threshold power density ~300 W cm$^{-2}$ [29]. This was attributed to improved processing that relied on EBL instead of conventional UV photolithography and the use of $SiO_2$ as a hard mask and a reduced microdisk diameter (1.2 vs. 3.5 μm in Ref. [16]) and hence a resulting smaller number of WGMs and a larger β value. Lasing was also linked to second-order radial modes, whose presence was made possible thanks to a small post diameter, which are less sensitive to sidewall roughness and ion damage occurring during the RIE step. Beyond those studies, Tabataba-Vakili et al. pointed out that the use of a bus WG is amenable with single-mode lasing operation, which would have to do with WGM selection taking place at the level of the whole PIC structure that involves a microdisk, a bus WG, and tethers [25], although those authors recently reported on two-mode lasing under pulsed excitation with such a PIC geometry [40].

One of the most systematic studies about the lasing characteristics of air-clad III-N microdisks was conducted by Sellés et al. on both AlN and GaN microdisks spanning a wide range of wavelengths, namely from the deep UV (275 nm) to the blue spectral range (470 nm), under pulsed optical excitation [30, 109]. Depending on the targeted emission wavelength, the gain medium consisted of either binary GaN/AlN MQWs or InGaN/GaN MQWs. It was shown that, in the UV range, GaN/AlN QWs are better suited than their QD counterparts due to the detrimental role played by the excited states of large GaN dots that suppress the gain provided by small dots due to their strong absorption in the corresponding spectral range. This feature emanates from the large QD size distribution observed with GaN/AlN QDs that is not seen in the InAs/GaAs platform [30].

Spectroscopic studies indicate that GaN/AlN QWs are characterized by a narrower emission linewidth than GaN/AlN QDs and hence a smaller Stokes shift, which makes them a more suitable gain medium at those critical wavelengths that can exhibit an IQE of several tens of percent. Additionally, mode competition arising from the disk geometry (WG thickness and disk diameter) was invoked to explain the measured β factor of ~$4\times10^{-4}$ that also accounted for the IQE of the gain medium. The asymmetric lineshape of the lasing mode was ascribed to the pulsed excitation scheme that could be responsible for transients originating from either density-dependent or heating effects. The observed redshift of the lasing modes upon increasing pumping power above threshold was linked to photochemical effects such as those pointed out by Aharonovich et al. [93], but it is also likely reminiscent of the changes in the spectral signature of WGMs reported by Rousseau et al. [37], where the critical role played by surface states was highlighted, especially at room temperature when using short pumping wavelengths. Sellés et al. also pointed out that provided $Q_{exp}$ values in excess of 1000 are measured, the lasing threshold fluence did not depend on the disk diameter at a given lasing wavelength [109]. Similarly, the carrier density at threshold ($n_{thr}$) was estimated to be nearly lasing wavelength independent for a given gain medium quality provided the quantum-confined Stark effect characteristic of *c*-plane-oriented quantum heterostructures does not play any prominent role [109].

Room temperature lasing under continuous-wave optical pumping was also reported in the green spectral range, at $\lambda = 514$ nm, in ~1 μm diameter GaN microdisks with embedded InGaN/GaN MQWs with a threshold power density of ~1 kW cm$^{-2}$ [110]. By analyzing the input-output (I-O) curve using standard laser rate equations [111], a relatively high-β value for this geometry of 0.043 was extracted. It is likely due to the small number of WGMs overlapping with the optical gain bandwidth. Let us note that β values in excess of 0.1 have been reported in microdisks with a diameter in excess of 2 μm [99, 112], whose exact origin remains relatively unclear knowing the small FSR of these devices and hence the large number of competing modes. In any case, as will be recalled hereafter, connecting the high-β values deduced from a laser rate equation analysis of I-O curves to a Purcell factor ($F_p$) in excess of unity for conventional dielectric resonators such as those considered in this review, which exhibit room temperature lasing, is a misconception.

Besides QWs, InGaN QDs and so-called InGaN fragmented QWs have also been used as active gain medium leading to room temperature pulsed lasing in air-clad *c*-plane III-N microdisks [97, 113]. In particular, it was highlighted that lasing occurring in these samples was ultimately the result of a tradeoff between the carrier capture efficiency, which is related to the areal density of the active medium, and the radiative emission efficiency of the latter. It is usually characterized by a high IQE even at room temperature due to strong spatial localization of the carriers. It is noteworthy that, despite an expected lower $n_{thr}$ value in QD lasers [114], continuous-wave lasing occurring in III-N QD microdisks remains to be shown.

High-β lasing is a well-known feature of small footprint nanolasers such as high $\frac{Q}{V_m}$ ratio dielectric resonators sustaining a reduced number of cavity modes. In particular, in the past decade or so, PhC membrane nanocavities proved to be ideally suited to investigate the lasing transition in devices where neither a sharp increase in the intensity nor a clear linewidth narrowing in the emission spectrum is observed [115, 116]. In such a situation, basing an analysis on the sole conventional laser rate equations [111] becomes problematic due to the efficient coupling of spontaneous photon emission to the nanocavity mode, hence explaining the terminology high-β nanolaser, which is a source of noise in those devices that operate with a small average number of photons stored in the cavity mode (roughly between one and a few hundreds) [117]. Therefore, to obtain additional insights into the emission properties of high-β nanolasers, one is usually led to assess the threshold based on the statistical nature of the emitted light [115]. In other words, the evolution of the second-order intensity autocorrelation function at zero-time delay, i.e. $g^{(2)}(0)$, must be monitored as a function of input power density. When β is high, this quantity exhibits a transition from thermal or bunched photon statistics (i.e. chaotic photon emission), for which bunches of photons are emitted as a function of time – in which case $g^{(2)}(0) > 1$ – to coherent or random photon statistics, for which photons are randomly emitted as a function of time, i.e. $g^{(2)}(0) = 1$. Remarkably, the larger the β value is, the smoother is the lasing transition and hence the less defined is the threshold [118].

In the specific framework of III-N PhC membrane cavities, to date, lasing has only been reported in structures having the 1D PhC nanobeam cavity geometry, with all of them showing high-β lasing features [12–14]. Thus, Niu et al. have demonstrated room temperature lasing under pulsed optical pumping at ~450 nm with a threshold fluence down to 9.1 μJ cm$^{-2}$ in GaN PhC nanobeam cavities with a $Q_{exp}$ value ranging between 1300 and 1900, which rely on three fragmented InGaN/GaN QWs as gain medium. Using laser rate equations, these authors derived a β value of 0.94 for their structures. In Refs. [12, 14], the

authors have reported a systematic study of the lasing transition occurring in the 445–460 nm range under room temperature continuous-wave optical pumping in GaN PhC nanobeam cavities with a single InGaN QW gain medium exhibiting a $Q_{exp}$ value in excess of 2000 at transparency. To go beyond a rate equation analysis, which led to β values in excess of 0.7 at 300 K in those structures (Figure 14A and D), and in the absence of any obvious linewidth narrowing upon increasing input power density that is usually synonymous of onset of lasing (Figure 14B and E), a quantum optical characterization, coupled to microscopic laser modeling for the interaction between the 2D QW gain medium and the fundamental cavity mode, was conducted both at room temperature (Figure 14C and F) and at cryogenic ones [14]. Power-dependent $g^{(2)}(0)$ measurements performed with a Hanbury-Brown and Twiss (HBT) interferometer show a progressive transition from thermal emission to the Poisson (coherent) limit (Figure 14C) as reported previously in Refs. [115, 118] for L3-type GaAs PhC nanocavities containing InAs QDs characterized at cryogenic temperatures. One very important outcome of such power-dependent $g^{(2)}(0)$ measurements led on nanolasers with an extended gain medium like QWs is that the input power density at which the $g^{(2)}(0)$ function starts to exhibit a progressive decrease toward unity, which is associated with the coherent emission threshold region, i.e. that where stimulated emission takes over spontaneous emission, does not coincide with the intensity threshold position such as that deduced from laser rate equation analyses (Figure 15A and B) [119]. The difference between those two thresholds is all the more important that β gets closer to one. It may very well explain the large difference

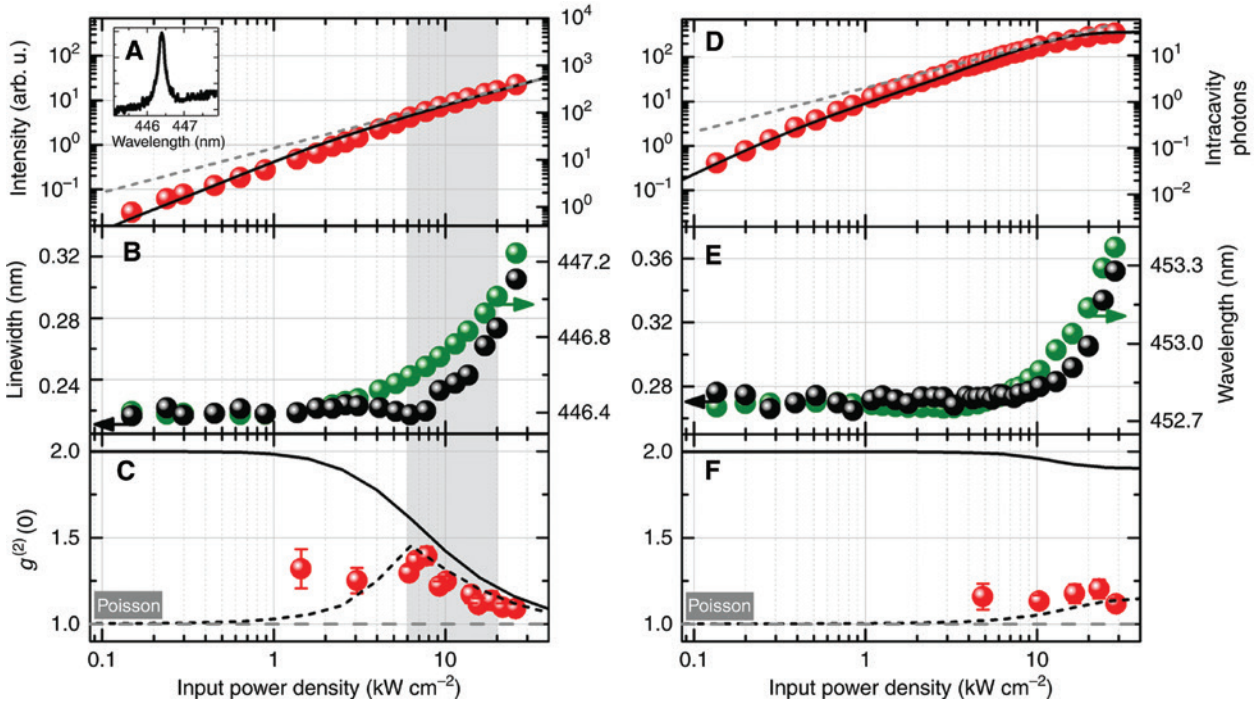


**Figure 14:** Room temperature optical and quantum-optical characterization of a lasing and nonlasing III-N nanobeam cavity. (A and D) Room temperature I-O curves. The theoretical model (solid line) in (A) shows a slight nonlinearity before converging to a slope of 1 (dashed line). (A, inset) Fundamental cavity mode at 0.64 kW cm$^{-2}$. The I-O characteristic in (D) is governed by nonradiative losses and does not show an s-bend before saturating. The increased output intensity with respect to (A) is indicative of an increase in light scattering toward the vertical direction. Note that the intracavity photon number is higher for the lasing nanobeam, which allows building up a coherent photon population. (B and E) Resonance peak wavelength (green) and linewidth (FWHM; black). Above 10 kW cm$^{-2}$, the development of resonance wavelength and emission linewidth is dominated by heating of the cavity region. The lasing structure in (B) exhibits a slight decrease in linewidth around $P \approx 5$ kW cm$^{-2}$. (C and F) Second-order autocorrelation function at zero time delay as obtained from experiment (data points) and theory. Proof of the transition to coherent emission (shaded excitation range) is provided by the power dependence of the deconvolved second-order autocorrelation data, showing a clear trend toward the Poisson limit ($g^{(2)}(0) = 1$) with increasing excitation power density. In contrast, the power dependence in (F) reveals a constant $g^{(2)}(0) \leq 1.2$. The evolution of the photon statistics is well reproduced by the microscopic theory (ideal, solid line; convolved, dashed line) when taking into account the calculated coherence time and the convolution with the temporal resolution (~225 ps) of the HBT setup. Error bars in (C and F) indicate the standard deviation obtained from fitting the recorded histograms that mirror $g^{(2)}(\tau)$. Reprinted from Ref. [14].

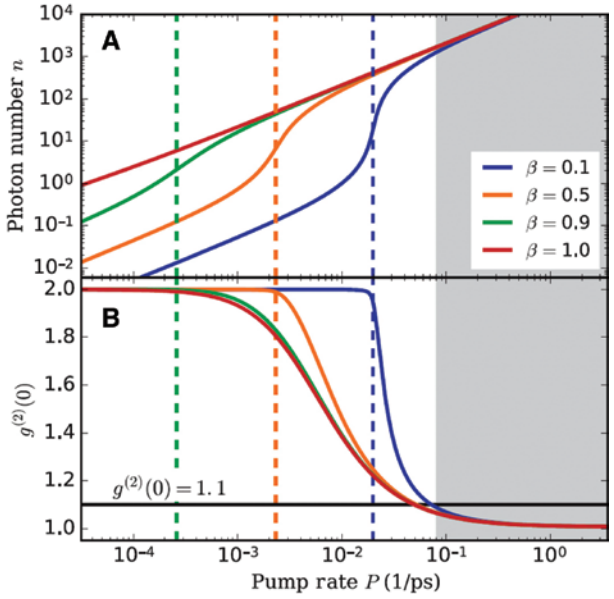


**Figure 15:** Input-output characteristics and degree of coherence of the emission of a nanolaser with an extended gain material, (A) output intensity and (B) $g^{(2)}(0)$ values are shown for different β. The large carrier number in the gain media is reflected in $N = 3 \times 10^4$, whereas the other parameters are the cavity decay rate $\kappa = 0.7$ p $s^{-1}$ and the light-matter interaction strength $g = 0.02$ p $s^{-1}$. For all values of β, the intensity threshold (dashed vertical lines) is clearly separated from the transition to coherent emission (gray area). Furthermore, the coherence thresholds indicate that increasing β has no benefit in terms of reducing the pump power to reach coherent emission. Reprinted with permission from Ref. [119]. Copyright (2018) American Physical Society.

in the quoted threshold power densities reported in Refs. [12] and [14], with values that roughly differ by one order of magnitude, for the very same 1D GaN PhC nanobeam structures. The evolution of the $g^{(2)}(0)$ function as a function of input power density is accompanied by an increase in coherence time from ~1 to ~800 ps across the lasing transition region based on the above-mentioned microscopic laser modeling [14]. Another relevant aspect of this study is related to the fact that for high-β nanolasers operating under realistic device conditions, i.e. for which nonradiative recombinations cannot be ignored, the estimated mean intracavity photon number at the coherent emission threshold is larger than 1, as what really matters is the imbalance between photons of stimulated and spontaneous origin (Figure 14A).

Finally, let us note that temperature-dependent I-O curves measured on those 1D GaN PhC nanobeam cavity lasers reveal a complex interplay between the 0D and 2D nature of the InGaN/GaN QW gain medium. Such a signature manifests itself through a thresholdless I-O curve measured at ~160 K despite an extracted β value less than unity. It can be related to a progressive quenching of nonradiative loss channels with decreasing temperatures. However, the observed inversed S-shaped I-O curves at lower temperatures was ascribed to the contribution of localized (0D) states typical of InGaN/GaN QWs that would contribute to the gain in the low excitation regime [14]. As at room temperature, at those cryogenic temperatures the only way to prove that a transition toward Poissonian emission statistics effectively takes place consists of monitoring the evolution of the $g^{(2)}(0)$ function as a function of input power density, hence showing that quantum-optical investigations are critical to demonstrate lasing in the $\beta \rightarrow 1$ regime.

# 4 Forthcoming challenges and novel fields of application

The previous sections showed that the field of III-N microresonators and nanoresonators evolved at a fast pace in the past few years, and as such, it will most likely be confronted to novel challenges. Hereafter, we have chosen to highlight some topics that are commonly addressed when dealing with dielectric resonators with embedded quantum nanostructures. We have also identified some emerging fields of application that are by no means exhaustive but rather illustrative of the potential of those optical resonators.

## 4.1 Vertical light extraction

The first relevant topic deals with light extraction from III-N resonators. Indeed, light emission mostly occurs within the membrane plane, which can require some specific experimental configurations to implement an efficient light collection scheme especially for experiments that are conducted at cryogenic temperatures. In this regard, it is worth mentioning that in-plane light collection through tapered optical fibers is not, to say the least, a well-established approach in the UV to blue spectral range for some obvious geometrical reasons. In fact, there is often the need to extract the light vertically, i.e. perpendicularly to the membrane plane. Thus, some recent demonstrations of III-N PICs relied on the use of grating outcouplers positioned at the extremity of bus WGs to ensure efficient vertical extraction of guided light with simulated outcoupling efficiencies of 3%–7% in the 400–420 nm spectral range for GaN-based structures on the one hand [25] and measured values up to 9% at 380 nm for AlN ones on the other [120]. A promising strategy to increase those numbers would consist of engineering grating outcouplers based on the inverse design

technique that recently proved to be extremely powerful for improving the overall performance of integrated photonic components [121, 122]. For small footprint 2D PhCs, it was recently shown that holes next to the cavity can be precisely tailored to promote vertical light emission [70, 123]. It consists of doubling the periodicity of those holes, which play the role of an extractor structure, compared to that of the PhC lattice to fold back the Fourier components of the electric field inside the light cone. A somewhat similar strategy has been proposed by Rousseau et al., which consists of forming a sidewall Bragg cross-grating in 1D GaN PhC nanobeam cavities operating in the blue spectral range that subsequently acts as vertical far-field coupler (Figure 16A) [31]. Using 3D-FDTD simulations, an increase in the vertical light extraction by up to three orders of magnitude was predicted compared to straight sidewalls, i.e. unmodified, ideal nanobeam cavities. An experimental investigation focusing on the evolution of the $Q_{exp}$ value and the far-field intensity as a function of the cross-grating coupler amplitude revealed that the average quality factor remains unaffected by the sidewall modulation while exhibiting up to a ninefold average increase in integrated far-field emission intensity, due to partial back-folding of the mode profile to $k=0$ induced by the subharmonic sidewall modulation, compared to unmodulated nanobeam structures (Figure 16B) [31]. Such a geometry should prove extremely beneficial in photon counting experiments requiring long integration times, and hence a high signal-to-noise ratio, such as the above-mentioned second-order intensity autocorrelation function measurements. Let us note that, contrary to their PhC counterparts, there is presently a lack of similar strategy for isolated small footprint III-N microdisks operating in the UV to visible range likely because a solution such as that implemented in the far-infrared to promote vertical light emission from WGMs in microdisks [124] could hardly be adapted to short wavelengths.

## 4.2 Electrical injection

Next to vertical light extraction, electrical injection is an obvious topic of wide interest to promote the eventual adoption of III-N PICs or the merger of III-N resonators, e.g. with Si photonics. As far as the two geometries considered in this review are concerned, a few demonstrations have been reported with the microdisk structure but most of the time on devices with a significantly larger footprint than the structures we are focusing on (diameter >> 10 µm vs. <10 µm here) and with a design that is not necessarily of the air-clad type. Among them, we can cite the case of spiral-shaped GaN-based microdisk lasers grown on *c*-plane sapphire susbtrate having a radius in excess of 50 µm and sandwich-like InGaN microring lasers grown on Si substrate with an external radius of 20 µm that both exhibit room temperature lasing under pulsed current-injection conditions [125, 126]. The geometry the closest to the structures of interest for this work has been reported by Tabataba-Vakili et al., who showed electroluminescence from wide GaN microrings that are part of a PIC [127]. In each case [125–127], the authors did not observe any WGMs below threshold, which was tentatively ascribed to the

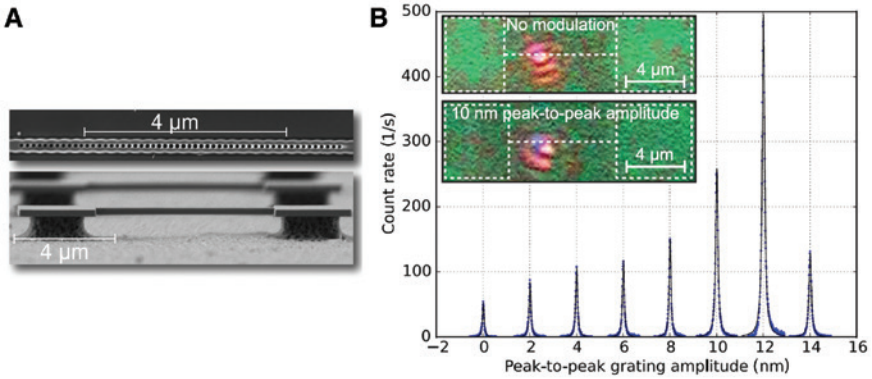


**Figure 16:** Structural and optical features of 1D GaN PhC nanobeam cavities with a single InGaN QW having a sidewall Bragg cross-grating far-field coupler for vertical light extraction.
(A) SEM images of III-N nanobeams on Si. (Top) Overhead view of a nanobeam cavity incorporating a cross-grating coupler. (Bottom) Air gap of ≈750 nm measured at 85° tilt. (B) Representative peaks showing the evolution of blue-shifted resonance with cross-grating peak-to-peak amplitude. Data and fits are shown with the background subtracted and are zeroed and shifted horizontally by the cross-grating peak-to-peak amplitude (in nm) for clarity. The insets show microscope CCD images recorded during µPL spectroscopy. The UV pump laser is seen as red, whereas the nanobeam emission is blue. The offset from the nanobeam center is an artifact of the setup. The nanobeam edges are outlined for clarity. Adapted with permission from Ref. [31]. Copyright (2016) AIP Publishing.

small FSR in these large diameter microdisk devices and the resulting strong competition between the different families of modes. Unlike their microdisk counterparts, electroluminescence has not been demonstrated in III-N PhC membranes yet, which is likely related to the stringent requirements in terms of mode volume and efficient lateral injection of carriers in such structures. Let us note that, in PhC membranes made from III-V semiconductors, electrical injection in 2D PhC lasers relied on either a lateral *p-n* junction obtained via ion implantation and/or impurity diffusion [128, 129], which remains a challenging strategy to implement in the III-N platform, or a more conventional vertical *p-n* junction design [130]. 1D InP-based PhC nanobeam cavity LDs have also been reported that relied on either the use of central posts enabling hole injection, hence circumventing issues due to the short diffusion length of the latter [131], or a complex heterogeneous integration to an Si-WG circuitry [132]. As mentioned earlier, the dual constraint, which consists of keeping a thin enough WG to have fewer cavity modes competing against each other while ensuring efficient hole injection, will likely call in favor of the use of a buried tunnel junction [11] in forthcoming electrically driven III-N PhC membrane cavities. In this respect, one could envision, for example, 1D PhC nanobeam cavities with support pads covered by a top metal electrode allowing for efficient lateral electron injection and hence hole generation in the cavity region. It would avoid the detrimental use of *p*-type GaN contacts whose contact resistance is quite high, typically in the $10^4$ Ω cm$^2$ range [11], and for which the layer resistivity remains on the order of a few tenths of Ω cm in good quality GaN [133], and likely much more for thin GaN WGs grown on Si. Another benefit from buried tunnel junctions deals with the expected decrease in the WG losses due to the lower residual absorption losses that are known to be mostly due to the *p*-type doped region in GaN-based edge emitting laser diodes [134, 135].

## 4.3 CQED with III-N photonic cavities

Another aspect of relevant interest when using high $\frac{Q}{V_m}$ ratio dielectric resonators, such as those considered in this work, which requires some clarification in view of forthcoming studies about high-β lasing and CQED studies, deals with the improper univocal link often made between a high spontaneous emission coupling factor and the enhancement of the spontaneous emission rate via the Purcell effect especially when leading room temperature studies. First of all, let us recall that a high-β value can be obtained in dielectric nanolasers without involving an $F_P$ value in excess of unity in situations where the FSR is on the order of or larger than the optical gain bandwidth, in which case values of $\beta > 0.1$ are only stemming from a pure geometrical origin [111]. This is the case, for example, in 1D PhC nanobeams that sustain a very small number of optical modes, typically ≤2, in which efficient spontaneous photon emission funneling into the lasing mode takes place [12, 14, 116]. The reason why $F_P < 1$ has to do with the fact that, at room temperature, high-β dielectric resonators operate in the broad emitter regime, i.e. $\Delta\omega_{em} >> \Delta\omega_{cav}$, where $\Delta\omega_{em}$ is the emitter linewidth, be it an inhomogeneously broadened light source like InGaN QWs or a homogeneously broadened single QD, and $\Delta\omega_{cav}$ is the cavity mode linewidth. In such a case, the original expression of $F_P$ derived for the situation where a cavity mode is on resonance with a two-level system, located at the maximum of the electric field in the cavity, whose dipole is aligned with the polarization of this cavity mode, given by [136]

$$F_P = \frac{3}{4\pi^2}\frac{\lambda_{cav}^3}{n^3}\frac{Q_{cav}}{V_m}, \tag{2}$$

where $\lambda_{cav}$ is the cavity mode wavelength and $Q_{cav}$ is the quality factor of the cavity mode, has to be modified into a generalized $F_P$ ($F_{P,gen}$) (see, e.g. Refs. [137, 138] and references therein). We therefore have

$$F_{P,gen} = \frac{3}{4\pi^2}\frac{\lambda_{cav}^3}{n^3}\frac{Q_{eff}}{V_m}, \tag{3}$$

where

$$\frac{1}{Q_{eff}} = \frac{1}{Q_{cav}} + \frac{1}{Q_{em}}, \tag{4}$$

is the effective quality factor that also depends on the emitter quality factor given by $Q_{em} = \frac{\omega_{cav}}{\Delta\omega_{em}}$ (on resonance), where $\omega_{cav}$ is the angular frequency of the cavity mode. Following this clarification, we can point out that the recent progress made with the fabrication of 1D GaN PhC nanobeam cavities for which $Q_{exp}$ values of ~8000 have been reported (Figure 17A) should allow to explore the mechanisms of coherent emission in nanolasers with extended gain media such as InGaN QWs from a situation where the β value has little impact on the pump rate at the coherence threshold ($P_{coh}$), corresponding, for example, to a $Q_{exp}$ value of ~2000 (cf. the vertical solid line in Figure 17B that illustrates the samples studied in Refs. [12, 14]), to a regime akin to that observed with a small number

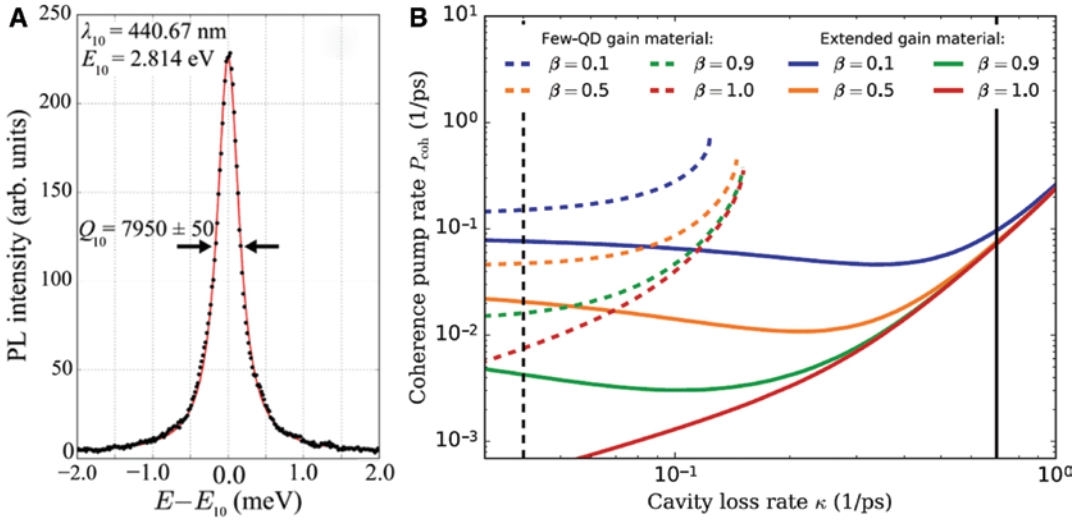


**Figure 17:** Optical properties of a state of the art 1D GaN PhC nanobeam cavity operating in the blue spectral range and link between the cavity loss rate and the coherence pump rate for 0D and 2D gain materials.
(A) High-resolution μPL spectrum of a KOH-etched nanobeam sample with $Q_{10} = 7950 \pm 50$ at 440.67 nm measured using 10 kW cm$^{-2}$ resonant pumping at 4 K, above the transparency threshold of the QW. (B) Pump rate $P_{coh}$ at the coherence threshold as a function of cavity loss rate $\kappa$. Parameters ($N$, $g$) correspond to those in Figure 1 (dashed) of Ref. [119] and Figure 15A and B (solid). Vertical lines indicate respective values for $\kappa$. One observes the different dependence on $\beta$ for the two cases as well as the transition between the regimes for varying $\kappa$. For a small number of emitters, there is an upper bound for $\kappa$ beyond which lasing cannot be achieved; thus, the dashed lines terminate above a certain value. (B) Reprinted with permission from Ref. [119]. Copyright (2018) American Physical Society.

of emitters like QDs where $P_{coh}$ varies by several orders of magnitude for $\beta \in$ 0.1–1 (Figure 17B) [119]. In particular, we should expect an alteration of β when switching from unmodulated nanobeam structures to structures incorporating a sidewall cross-grating coupler without modifying the $Q_{exp}$ value [31]. Such a feature would not be easily accessible at room temperature with other platforms, but it would require an efficient passivation of surface states possibly through a combination of atomic layer etching, which has already been successfully applied to the case of Si [139] and InGaAs [140] materials, to clean the exposed surface after processing and ALD using appropriately chosen precursors to encapsulate the 1D PhC nanobeams. Note that such studies could be led at cryogenic temperatures before their investigation at 300 K.

In addition to the enhancement of the spontaneous emission rate due to the Purcell effect that could be obtained at cryogenic temperatures in high $\frac{Q}{V_m}$ ratio III-N resonators with suitably positioned narrow linewidth emitters, such as the NIR telecom range SPEs investigated by Zhou et al. [10], another CQED topic triggering significant interest that could be tackled using the present III-N structures deals with the strong coupling regime between a cavity mode and an individual two-level quantum emitter such as QDs or appropriate point defects. Building upon the seminal work by Andreani et al. [141] and the review article by Khitrova et al. [142], we can determine the requirements in terms of $Q_{exp}$ value to achieve the strong coupling regime for a system operating in the good emitter regime, i.e. such that $\Delta\omega_{em} << \Delta\omega_{cav}$ [143]. Thus, at zero detuning, which corresponds to the emitter and the cavity mode being on resonance, we should ensure that the normal mode splitting $\Omega = 2g$ of the system eigenmodes, where $g = \frac{\mu E_{vac}}{\hbar}$ is the quantum emitter-cavity light field coupling strength, is indeed larger than the linewidths of the coupled system resonances equal to $\frac{[\gamma + \kappa]}{2}$, where $\mu$ is the dipole moment of the single emitter, $E_{vac} = \frac{1}{n}\left[\frac{\hbar\omega_{cav}}{2\varepsilon_0 V_m}\right]^{1/2}$ is the vacuum field amplitude, $\hbar$ is the reduced Planck constant, $\varepsilon_0$ is the permittivity of free space, and $\gamma$ and $\kappa$ are the homogeneous decay rates of the quantum emitter and the cavity mode, respectively. When following the steps described in Ref. [142] in the situation where $\gamma$ is dominated by the Purcell effect (i.e. $\gamma \approx F_P \gamma_{em}$, where $\gamma_{em}$ is the radiative decay rate of the bare emitter), we can show, after some straightforward calculations, that $Q_{exp}$ should verify the following inequality:

$$Q_{exp} > \frac{\lambda_{cav}^{3/2}}{\mu}\left[\frac{\varepsilon_0 \hbar\omega_{cav}}{2n}\right]^{1/2}, \quad (5)$$

where we considered a representative mode volume $V_m = \left(\frac{\lambda_{cav}}{n}\right)^3$ and we made use of the conventional

**Table 2:** Selected challenges to be tackled with III-N photonic cavities.

| Challenge | Solution(s) | Expected outcome(s) | Application(s) |
|---|---|---|---|
| Vertical light extraction | Sidewall cross-grating coupler (1D) | Increased vertical light emission | Optical measurements [$g^{(2)}(\tau)$ measurements, etc.] |
| | Hole extractor structure in 2D membranes | | |
| | Grating outcoupler based on inverse design | | |
| Electrical injection | Buried tunnel junction for efficient lateral hole injection | Lower WG losses and lower series + contact resistances | Nanophotonic emitters, including nanolaser diodes |
| CQED | Preselected two-level emitter controlled in position | Enhanced light-matter coupling | Purcell effect studies, including QD nanolasers |
| | | | Strong coupling regime studies |

relationship linking the bare emitter lifetime $\tau_{em}$ and $\mu$ recalled in Ref. [144]:

$$\gamma_{em} = \frac{1}{\tau_{em}} = \frac{n\omega_{em}^3 \mu^2}{3\pi\varepsilon_0 \hbar c^3}, \quad (6)$$

keeping in mind that here $\omega_{em} = \omega_{cav}$. Hence, assuming a reasonable radiative emitter lifetime of 1 ns at $\gamma = 450$ nm, we then obtain $Q_{exp} > 7400$, a value that is clearly within reach for 1D GaN PhC nanobeam cavities (Figure 17A). Let us point out that the significantly larger $Q_{exp}$ values reported in the NIR, e.g. with 1D AlN PhC nanobeam cavities [49], could potentially allow for strong coupling observations with appropriate point-defect-like quantum emitters operating in this spectral range.

For the sake of clarity, the challenges of relevant interest when dealing with III-N photonic cavities discussed in the previous subsections are listed in Table 2.

## 4.4 Emerging applications

Beyond the above-mentioned subjects, other emerging areas would certainly be worth being applied to the present III-N membrane resonators. One such example is that of so-called two-laser Raman thermometry, which can probe both thermal conductivity and thermal field mapping in a contactless, and hence in a nondestructive, manner [145, 146]. In such an experiment, a high-power fixed laser is used as a heat source, whereas a second low-power laser scans the sample to probe the local temperature by precisely monitoring the spectral position of a known Raman active mode. Using a 488 nm probe laser, a spatial resolution reaching 300 nm together with a high-temperature accuracy, down to ±2 K, was reported [145]. As an illustration of the potential of this technique, using conventional one-beam Raman experiment, Jagsch et al. showed by following the redshift of the polar $A_1$(LO) phonon peak as temperature sensor that the increasing cavity mode linewidth broadening reported at room temperature with increasing pumping power density in high-β 1D GaN PhC nanobeam cavity lasers originated from a temperature increase of the cavity by about 50–80 K in the high excitation range [14]. With the two-laser Raman thermometry technique, it would become possible to determine the profile of the thermal field decay, e.g. distinguish the diffusive limit when the membrane experiences a small temperature gradient, which is characterized by a ln($d$) dependence of the temperature with increasing distance $d$ from the excitation spot, from an exponential decay in the case of large temperature gradients [145]. The impact of geometrical parameters such as holes on the thermal field decay could be clearly quantified. It would certainly prove extremely beneficial to optimize large surface-to-volume ratio III-N nanophotonic devices for their subsequent integration to more advanced PICs. Furthermore, multicausal origins to linewidth broadening phenomena (photodesorption, etc.) could be better understood if the specific impact of temperature could be clearly isolated.

Another field with a significant potential deals with piezo-acousto-optic experiments carried out with high-$Q$ 1D AlN PhC nanobeam cavities that have been engineered in both photonic and acoustic domains [147, 148]. By taking advantage of the piezoelectric properties of III-N semiconductors, the acousto-optic modulation of those nanocavities was reported in the GHz frequency range with a mechanical frequency of 3.18 GHz being achieved in a structure having a C-band optical $Q_{int}$ value of 120,000 and a mechanical $Q$ ($Q_{mech}$) in excess of 10,000 at 2.5 K (>3000 at 300 K) on the one hand [147] and a modulation up to a frequency of 19 GHz, corresponding to the microwave K band, in a nanobeam device characterized by a nearly equivalent C-band optical $Q_{int}$ value of 110,000 on the other hand [148]. One of the challenges when designing such structures consists of obtaining simultaneously a photonic bandgap and an acoustic quasi-bandgap with

high-$Q$ values, hence requiring precise structure engineering. In particular, it was pointed out that undesired mechanical deformation such as buckling in uniaxially strained nanobeams should be avoided via an appropriate design of the support pads to release the accumulated stress along the suspended PhC structure [147]. In the same vein, the membrane thickness will ultimately determine the resonance frequency when targeting very high microwave frequencies, the thinner it is, the higher is the frequency [148]. The exploitation of such optomechanical nanoresonators is still in its infancy, but they may prove instrumental for both fundamental and applied studies with topics including, but obviously not restricted to, nonreciprocal and break time-reversal symmetry studies in photonic systems [149] and coherent signal processing, opto-acoustic oscillators, and mechanical sensors, respectively [147]. In this respect, let us note that Bochmann et al. have achieved electromechanically induced optical transparency stemming from coherent interactions between microwave, mechanical, and optical modes using a suspended high-$Q$ 1D AlN optomechanical crystal with Al electrodes and an AlN photonic circuit (Figure 18) [150]. Their AlN nanobeam photonic structure features an optical $Q_{int}$ value of 130,000 in the C-band and a $Q_{mech}$ value of 2500 at room temperature at the resonance frequency $\omega_m/2\pi = 4.24$ GHz, which matches the operating frequency of superconducting quantum bits (qubits). Such on-chip demonstration could therefore enable coherent quantum state transfer from the microwave to the optical spectral range while offering long-range quantum

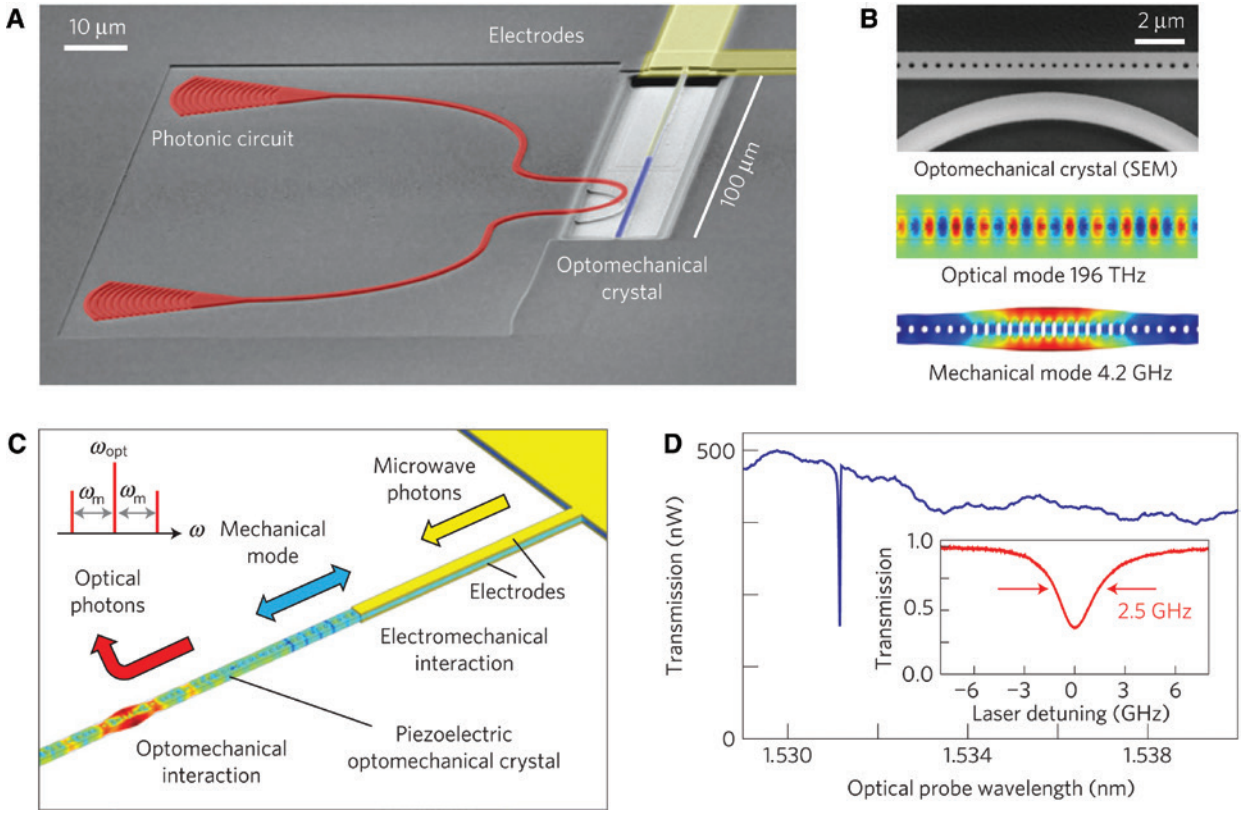


**Figure 18:** Device and electro-optomechanical coupling scheme.
(A) SEM of the device (angled view) showing the mechanically suspended AlN optomechanical crystal (blue) with aluminum electrodes (yellow) and the AlN photonic circuit (red, rib WG, and grating couplers). (B) Top view of the central region of the optomechanical crystal (SEM) and numerical simulations of the electrical field distribution of the optical mode at $\omega_{cav}/2\pi = 196$ THz and the mechanical displacement profile of the localized mechanical breathing mode at $\omega_m/2\pi = 4.2$ GHz. (C) Schematic of electro-optomechanical transduction in the piezoelectric optomechanical crystal (light blue). An electrical microwave signal on the electrodes (yellow) induces strain by piezoelectric coupling and resonantly excites the engineered breathing mode of the optomechanical crystal. Parametric optomechanical coupling to the colocalized optical mode (not shown) generates optical sidebands on a probe laser field (schematic; top left), thereby upconverting the mechanical (electrical) state to optical frequencies. Color coding of the suspended beam indicates mechanical displacement of the electrically driven device (numerical simulation). (D) Measured optical transmission as a function of optical probe wavelength. The PhC resonance at 1531.5 nm has a linewidth $\kappa/2\pi = 2.5$ GHz full-width at half-maximum with resonant transmission $T = 37\%$ (inset). Reprinted with permission from Ref. [150]. Copyright (2013) Springer-Nature.

network capabilities in novel superconducting qubit circuit architectures.

Because of its likely more long-term development, we briefly mention the potential of III-N resonators for the field of optogenetics [15]. First, let us point out that 1D GaAs nanobeam cavities with embedded QDs have already been successfully used to probe *in vitro* proteins inside single cells, hence indicating that this type of nanophotonic devices offers possibilities to explore cell biology with novel insights [151]. In this regard, the reduced cytoxicity of III-N and the ability to engineer III-N nanophotonic structures emitting in the near-UV to green spectral range make this system a very appealing platform for optogenetic studies with minimal invasiveness compared to solutions currently implemented, e.g. for optogenetic stimulation experiments [152]. Among the future directions identified to improve existing optical neural interfaces, the miniaturization of existing light sources enabling the optical stimulation with single-cell resolution in freely behaving mammals is of high interest [153]. A major asset of such low footprint light sources would be the possibility to address individual cells with an unprecedented spatial control, hence allowing for more selective optogenetic activation and silencing experiments. Despite their reduced light output power, those devices would most certainly be ideally suited for the readout and control of bistable step-function channelrhodopsin derivatives that offer a light sensitivity increased by orders of magnitude to expressing cells [154]. With the ongoing downsizing of wireless optical-neural interfaces for light delivery to brain tissue in freely moving mammals, nearly lifelong *in vivo* experiments could be carried out, hence allowing an unprecedented monitoring of the neural activity as a function of the aging status of the brain. In particular, the use of parallelized nanophotonic structures emitting at different wavelengths that would target proteins made sensitive to different colors would most certainly open new pathways to unravel the complex processes taking place in living cells.

# 5 Conclusion

Through this review, we have demonstrated that, thanks to their fast growing technological maturity, small footprint III-N membrane resonators can nowadays exhibit optical quality factors mostly limited by surface absorption in the visible range and residual bulk absorption in the NIR, a general feature that was most certainly considered as out of reach when the first heteroepitaxial structures of this type were realized 15 years ago. This has been made possible thanks to the combination of a genetic algorithm automated process and the progress made in terms of sample processing, e.g. via the introduction of a single-step pattern transfer. The broad spectral tuning range and the possibility to fabricate both active and passive devices with this material platform allow to explore a breadth of applications. The demonstration of room temperature blue lasing under continuous-wave optical pumping in both GaN microdisks and 1D GaN PhC nanobeam cavities and the recent advent of PICs open promising pathways for the realization of a novel generation of compact devices operating under electrical injection. Beyond structures exhibiting larger SHG and THG conversion efficiencies, we pointed out that foreseeable demonstrations within the next few years could include the report of the Purcell effect at cryogenic temperature using suitably positioned quantum emitters and potentially the strong coupling regime as well. High-β III-N nanolasers also promise to be an exciting platform to unravel the complexity of photon statistic properties when those sources are subjected to unconventional excitation regimes.

# Supplementary Material

See supplementary material for additional information on (Section 1) thin $SiO_2$ film coating of air-clad III-N microdisks and PhC nanocavities and (Section 2) gas tuning of PhC nanobeam cavities.

**Acknowledgments:** The authors would like to thank Noelia Vico Triviño, Ian Rousseau, Momchil Minkov, Jean-François Carlin, Vincenzo Savona, and Romuald Houdré for their essential contributions and fruitful discussions over the years for the work done at École Polytechnique Fédérale de Lausanne. Fruitful collaborations with the groups of Stephan Reitzenstein at the Technische Universität Berlin, Frank Jahnke and Christopher Gies at the University of Bremen, Matteo Galli at the Università di Pavia, and Massimo Gurioli at the University of Florence are also deeply acknowledged.

**Funding:** This work was supported by the Swiss National Science Foundation (grants. 200020_162657, Funder Id: http://dx.doi.org/10.13039/501100001711 and 200020_182442).

# References

[1] Akasaki I. Nobel lecture: fascinated journeys into blue light. Rev Mod Phys 2015;87:1119–31.

[2] Amano H. Nobel lecture: growth of GaN on sapphire via low-temperature deposited buffer layer and realization of p-type GaN by Mg doping followed by low-energy electron beam irradiation. Rev Mod Phys 2015;87:1133–38.
[3] Nakamura S. Nobel lecture: background story of the invention of efficient blue InGaN light emitting diodes. Rev Mod Phys 2015;87:1139–51.
[4] Feneberg M, Neuschl B, Thonke K, et al. Sharp bound and free exciton lines from homoepitaxial AlN. Phys Stat Solid A 2011;208:1520–2.
[5] Paschotta R. Encyclopedia of laser physics and technology. Berlin: Wiley-VCH, 2008.
[6] Jung H, Tang HX. Aluminum nitride as nonlinear optical material for on-chip frequency comb generation and frequency conversion. Nanophotonics 2016;5:263–71.
[7] Christopoulos S, Baldassarri Höger von Högersthal G, Grundy AJD, et al. Room-temperature polariton lasing in semiconductor microcavities. Phys Rev Lett 2007;98:126405.
[8] Christmann G, Butté R, Feltin E, Carlin J-F, Grandjean N. Room temperature polariton lasing in a GaN/AlGaN multiple quantum well microcavity. Appl Phys Lett 2008;93:051102.
[9] Holmes MJ, Choi K, Kako S, Arita M, Arakawa Y. Room-temperature triggered single photon emission from a III-nitride site-controlled nanowire quantum dot. Nano Lett 2014;14:982–6.
[10] Zhou Y, Wang Z, Rasmita A, et al. Room temperature solid-state quantum emitters in the telecom range. Sci Adv 2018;4:eaar3580.
[11] Malinverni M, Tardy C, Rossetti M, et al. InGaN laser diode with metal-free laser ridge using $n^+$-GaN contact layers. Appl Phys Express 2016;9:061004.
[12] Vico Triviño N, Butté R, Carlin J-F, Grandjean N. Continuous wave blue lasing in III-nitride nanobeam cavity on silicon. Nano Lett 2015;15:1259–63.
[13] Niu N, Woolf A, Wang D, et al. Ultra-low threshold gallium nitride photonic crystal nanobeam laser. Appl Phys Lett 2015;106:231104.
[14] Jagsch S, Vico Triviño N, Callsen G, et al. A quantum optical study of thresholdless lasing features in high-β nitride nanobeam cavities. Nat Commun 2018;9:564.
[15] Dance A. Micromanagement with light. Nature 2015;528:291–4.
[16] Haberer ED, Sharma R, Meier C, et al. Free-standing, optically pumped, GaN/InGaN microdisk lasers fabricated by photoelectrochemical etching. Appl Phys Lett 2004;85:5179–81.
[17] Choi Y-S, Hennessy K, Sharma R, et al. GaN blue photonic crystal membrane nanocavities. Appl Phys Lett 2005;87:243101.
[18] Rousseau I, Sánchez-Arribas I, Shojiki K, Carlin J-F, Butté R, Grandjean N. Quantification of scattering loss of III-nitride photonic crystal cavities in the blue spectral range. Phys Rev B 2017;95:125313.
[19] Arita M, Ichida S, Kako S, Iwamoto S, Arakawa Y. AlN air-bridge photonic crystal nanocavities demonstrating high quality factor. Appl Phys Lett 2007;91:051106.
[20] Tamboli AC, Schmidt MC, Hirai A, DenBaars SP, Hu EL. Observation of whispering gallery modes in nonpolar m-plane GaN microdisks. Appl Phys Lett 2009;94:251116.
[21] Bürger M, Ruth M, Declair S, Förstner J, Meier C, As DJ. Whispering gallery modes in zinc-blende AlN microdisks containing non-polar GaN quantum dots. Appl Phys Lett 2013;102:081105.
[22] Krost A, Dadgar A. GaN-based optoelectronics on silicon substrates. Mater Sci Eng B Solid 2002;93:77–84.
[23] Brunner D, Angerer H, Bustarret E, et al. Optical constants of epitaxial AlGaN films and their temperature dependence. J Appl Phys 1997;82:5090–6.
[24] Vico Triviño N, Dharanipathy U, Carlin J-F, Diao Z, Houdré R, Grandjean N. Integrated photonics on silicon with wide bandgap GaN semiconductor. Appl Phys Lett 2013;102:081120.
[25] Tabataba-Vakili F, Doyennette L, Brimont C, et al. Blue microlasers integrated on a photonic platform on silicon. ACS Photonics 2018;5:3643–8.
[26] McCall SL, Levi AFJ, Slusher RE, Pearton SJ, Logan RA. Whispering-gallery mode microdisk lasers. Appl Phys Lett 1992;60:289–91.
[27] Gayral B, Gérard JM, Lemaître A, Dupuis C, Manin L, Pelouard JL. High-Q wet-etched GaAs microdisks containing InAs quantum boxes. Appl Phys Lett 1999;75:1908–10.
[28] Borselli M, Johnson TJ, Painter O. Beyond the Rayleigh scattering limit in high-Q silicon microdisks: theory and experiment. Opt Express 2005;13:1515–30.
[29] Tamboli AC, Haberer ED, Sharma R, Lee KH, Nakamura S, Hu EL. Room-temperature continuous-wave lasing in GaN/InGaN microdisks. Nat Photonics 2007;1:61–4.
[30] Sellés J, Brimont C, Cassabois G, et al. Deep-UV nitride-on-silicon microdisk lasers. Sci Rep 2016;6:21650.
[31] Rousseau I, Sánchez-Arribas I, Carlin J-F, Butté R, Grandjean N. Far-field coupling in nanobeam photonic crystal cavities. Appl Phys Lett 2016;108:201104.
[32] Simeonov D, Feltin E, Altoukhov A, et al. High quality nitride based microdisks obtained via selective wet etching of AlInN sacrificial layers. Appl Phys Lett 2008;92:171102.
[33] Puchtler TJ, Woolf A, Zhu T, Gachet D, Hu EL, Oliver RA. Effect of threading dislocations on the quality factor of InGaN/GaN microdisk cavities. ACS Photonics 2015;2:137–43.
[34] Vico Triviño N, Rossbach G, Dharanipathy U, et al. High quality factor two dimensional GaN photonic crystal cavity membranes grown on silicon substrate. Appl Phys Lett 2012;100:071103.
[35] Winters HF, Coburn JW. The etching of silicon with $XeF_2$ vapor. Appl Phys Lett 1979;34:70–3.
[36] Vicknesh S, Tripathy S, Lin VKX, Wang LS, Chua SJ. Fabrication of deeply undercut GaN-based microdisk structures on silicon platforms. Appl Phys Lett 2007;90:071906.
[37] Rousseau I, Callsen G, Jacopin G, Carlin J-F, Butté R, Grandjean N. Optical absorption and oxygen passivation of surface states in III-nitride photonic devices. J Appl Phys 2018;123:113103.
[38] Roland I, Zeng Y, Checoury X, et al. Near-infrared III-nitride-on-silicon nanophotonic platform with microdisk resonators. Opt Express 2016;24:9602–10.
[39] Roland I, Gromovyi M, Zeng Y, et al. Phase-matched second harmonic generation with on-chip GaN-on-Si microdisks. Sci Rep 2016;6:34191.
[40] Tabataba-Vakili F, Doyennette L, Brimont C, et al. Demonstration of critical coupling in an active III-nitride microdisk photonic circuit on silicon. Sci Rep 2019;9:18095.
[41] Weiss DS, Sandoghdar V, Hare J, et al. Splitting of high-Q Mie modes induced by light backscattering in silica microspheres. Opt Lett 1995;20:1835–7.
[42] Kouno T, Kishino K, Sakai M. Lasing action on whispering gallery mode of self-organized GaN hexagonal microdisk crystal fabricated by RF-plasma-assisted molecular beam epitaxy. IEEE J Quantum Electron 2011;47:1565–70.

[43] Baek H, Lee C-H, Chung K, Yi G-C. Epitaxial GaN microdisk lasers grown on graphene microdots. Nano Lett 2013;13:2782–5.
[44] Zhang Y, Zhang X, Li KH, Cheung YF, Feng C, Choi HW. Advances in III-nitride semiconductor microdisk lasers. Phys Stat Solid A 2015;212:960–73.
[45] Ren CX, Puchtler TJ, Zhu T, Griffiths JT, Oliver RA. Defects in III-nitride microdisk cavities. Semicond Sci Technol 2017;32:033002.
[46] Gottscho RA, Jurgensen CW, Vitkavage DJ. Microscopic uniformity in plasma-etching. J Vac Sci Technol B 1992;10:2133–47.
[47] Sergent S, Arita M, Kako S, Tanabe K, Iwamoto S, Arakawa Y. High-Q AlN photonic crystal nanobeam cavities fabricated by layer transfer. Appl Phys Lett 2012;101:101106.
[48] Néel D, Sergent S, Mexis M, et al. AlN photonic crystal nanocavities realized by epitaxial conformal growth on nanopatterned silicon substrate. Appl Phys Lett 2011;98:261106.
[49] Pernice WHP, Xiong C, Schuck C, Tang HX. High-Q aluminum nitride photonic crystal nanobeam cavities. Appl Phys Lett 2012;100:091105.
[50] Arita M, Kako S, Iwamoto S, Arakawa Y. Fabrication of AlGaN two-dimensional photonic crystal nanocavities by selective thermal decomposition of GaN. Appl Phys Express 2012;5:126502.
[51] Sergent S, Kako S, Bürger M, et al. Active zinc-blende III-nitride photonic structures on silicon. Appl Phys Express 2016;9:012002.
[52] Blumenthal S, Bürger M, Hildebrandt A, et al. Fabrication and characterization of two-dimensional cubic AlN photonic crystal membranes containing zincblende GaN quantum dots. Phys Stat Solid C 2016;13:292–6.
[53] Throughout this review, we adopt the effective mode volume definition introduced by Foresi et al. [54], namely $V_m = \frac{\int_\Omega \varepsilon(r)|E(r)|^2 d^3r}{\max[\varepsilon(r)|E(r)|^2]}$, where $\varepsilon(r)$ is the position-dependent dielectric constant and $E(r)$ is the position-dependent electric field.
[54] Foresi JS, Villeneuve PR, Ferrera J, et al. Photonic-bandgap microcavities in optical waveguides. Nature 1997;390:143–5.
[55] Zhang Z, Qiu M. Small-volume waveguide-section high Q microcavities in 2D photonic crystal slabs. Opt Express 2004;12:3988–95.
[56] Akahane Y, Asano T, Song B-S, Noda S. High-Q photonic nanocavity in a two-dimensional photonic crystal. Nature 2003;425:944–7.
[57] Minkov M, Savona V. Automated optimization of photonic crystal slab cavities. Sci Rep 2014;4:5124.
[58] Lai Y, Pirotta S, Urbinati G, et al. Genetically designed L3 photonic crystal nanocavities with measured quality factor exceeding one million. Appl Phys Lett 2014;104:241101.
[59] Dharanipathy UP, Minkov M, Tonin M, Savona V, Houdré R. High-Q silicon photonic crystal cavity for enhanced optical nonlinearities. Appl Phys Lett 2014;105:101101.
[60] Vico Triviño N, Minkov M, Urbinati G, et al. Gallium nitride L3 photonic crystal cavities with an average quality factor of 16 900 in the near infrared. Appl Phys Lett 2014;105:231119.
[61] Gorodetsky ML, Pryamikov AD, Ilchenko VS. Rayleigh scattering in high-Q microspheres. J Opt Soc Am B 2000;17:1051–7.
[62] Mexis M, Sergent S, Guillet T, et al. High quality factor nitride-based optical cavities: microdisks with embedded GaN/Al(Ga)N quantum dots. Opt Lett 2011;36:2203–5.
[63] Berkowicz E, Gershoni D, Bahir G, et al. Measured and calculated radiative lifetime and optical absorption of $In_xGa_{1-x}N$/GaN quantum structures. Phys Rev B 2000;61:10994–1008.
[64] Rousseau I. III-nitride semiconductor photonic nanocavities on silicon. Ph.D. thesis. EPFL, 2018.
[65] La China F, Intonti F, Caselli N, et al. Vectorial near-field imaging of a GaN based photonic crystal cavity. Appl Phys Lett 2015;107:101110.
[66] Caselli N, Intonti F, La China F, et al. Ultra-subwavelength phase sensitive Fano-imaging of localized photonic modes. Light Sci Appl 2015;4:e326.
[67] Andreani LC, Gerace D. Photonic-crystal slabs with a triangular lattice of triangular holes investigated using a guided-mode expansion method. Phys Rev B 2006;73:235114.
[68] Sam-Giao D, Néel D, Sergent S, et al. High quality factor AlN nanocavities embedded in a photonic crystal waveguide. Appl Phys Lett 2012;100:191104.
[69] Roland I, Zeng Y, Han Z, et al. Near-infrared gallium nitride two-dimensional photonic crystal platform on silicon. Appl Phys Lett 2014;105:011104.
[70] Sabry Mohamed M, Simbula A, Carlin J-F, et al. Efficient continuous-wave nonlinear frequency conversion in high-Q gallium nitride photonic crystal cavities on silicon. APL Photonics 2017;2:031301.
[71] Tabataba-Vakili F, Roland I, Checoury X, et al. Q factor limitation at short wavelength (around 300 nm) in III-nitride-on-silicon photonic crystal cavities. Appl Phys Lett 2017;111:131103.
[72] Slusher RE, Levi AFJ, Mohideen U, McCall SL, Pearton SJ, Logan RA. Threshold characteristics of semiconductor microdisk lasers. Appl Phys Lett 1993;63:1310–2.
[73] Shaklee KL, Leheny RF. Direct determination of optical gain in semiconductor crystals. Appl Phys Lett 1971;18:475–7.
[74] Dharanipathy UP, Vico Triviño N, Yan C, et al. Near-infrared characterization of gallium nitride photonic-crystal waveguides and cavities. Opt Lett 2012;37:4588–90.
[75] Talneau A, Lee KH, Guilet S, Sagnes I. Efficient coupling to W1 photonic crystal waveguide on InP membrane through suspended access guides. Appl Phys Lett 2008;92:061105.
[76] Parrain D, Baker C, Wang G, et al. Origin of optical losses in gallium arsenide disk whispering gallery resonators. Opt Express 2015;23:19656–72.
[77] Sekoguchi H, Takahashi Y, Asano T, Noda S. Photonic crystal nanocavity with a Q-factor of ~9 million. Opt Express 2014;22:916–24.
[78] Mandel L, Wolf E. Optical coherence and quantum optics. Cambridge: Cambridge University Press, 1995.
[79] Lumerical Solutions, Inc. Complex structures – Surface roughness, 2017.
[80] Johnson SG, Povinelli ML, Soljačić M, Karalis A, Jacobs S, Joannopoulos JD. Roughness losses and volume-current methods in photonic-crystal waveguides. Appl Phys B 2005;81:283–93.
[81] Vučković J, Lončar M, Mabuchi H, Scherer A. Design of photonic crystal microcavities for cavity QED. Phys Rev E 2001;65:016608.
[82] Van de Walle CG, Segev D. Microscopic origins of surface states on nitride surfaces. J Appl Phys 2007;101:081704.
[83] Landmann M, Rauls E, Schmidt WG, Neumann MD, Speiser E, Esser N. GaN m-plane: atomic structure, surface bands, and optical response. Phys Rev B 2015;91:035302.

[84] Reshchikov RA, Foussekis M, Baski AA. Surface photovoltage in undoped n-type GaN. J Appl Phys 2010;107:113535.
[85] Himmerlich M, Eisenhardt A, Shokhovets S, et al. Confirmation of intrinsic electron gap states at nonpolar GaN(1-100) surfaces combining photoelectron and surface optical spectroscopy. Appl Phys Lett 2014;104:171602.
[86] Portz V, Schnedler M, Eisele H, Dunin-Borkowski RE, Ebert Ph. Electron affinity and surface states of GaN m-plane facets: implication for electronic self-passivation. Phys Rev B 2018;97:115433.
[87] King SW, Barnak JP, Bremserm MD, et al. Cleaning of AlN and GaN surfaces. J Appl Phys 1998;84:5248–60.
[88] Bermudez VM, Long JP. Chemisorption of $H_2O$ on GaN(0001). Surf Sci 2000;450:98–105.
[89] Calarco R, Marso M, Richter T, et al. Size-dependent photoconductivity in MBE-grown GaN-nanowires. Nano Lett 2005;5:981–4.
[90] Cao XA, Pearton SJ, Zhang AP, et al. Electrical effects of plasma damage in p-GaN. Appl Phys Lett 1999;75:2569–71.
[91] Choi HW, Chua SJ, Raman A, Pan JS, Wee ATS. Plasma-induced damage to n-type GaN. Appl Phys Lett 2000;77:1795–7.
[92] Miikkulainen V, Leskelä M, Ritala M, Puurunen RL. Crystallinity of inorganic films grown by atomic layer deposition: overview and general trends. J Appl Phys 2013;113:021301.
[93] Aharonovich I, Niu N, Rol F, et al. Controlled tuning of whispering gallery modes of GaN/InGaN microdisk cavities. Appl Phys Lett 2011;99:111111.
[94] Niu N, Liu T-L, Aharonovich I, et al. A full free spectral range tuning of p-i-n doped gallium nitride microdisk cavity. Appl Phys Lett 2012;101:161105.
[95] Kouno T, Sakai M, Takeshima H, et al. Microsensors based on a whispering gallery mode in AlGaN microdisks undercut by hydrogen-environment thermal etching. Appl Opt 2017;56:3589–93.
[96] Jágerská J, Zhang H, Diao Z, Le Thomas N, Houdré R. Refractive index sensing with an air-slot photonic crystal nanocavity. Opt Lett 2010;35:2523–5.
[97] Aharonovich I, Woolf A, Russell KJ, et al. Low threshold, room-temperature microdisk lasers in the blue spectral range. Appl Phys Lett 2013;103:021112.
[98] Sergent S, Arita M, Kako S, Tanabe K, Iwamoto S, Arakawa Y. High-Q AlN ladder-structure photonic crystal nanocavity fabricated by layer transfer. Phys Stat Solid C 2013;10:1517–20.
[99] Bürger M, Callsen G, Kure T, et al. Lasing properties of nonpolar GaN quantum dots in cubic aluminum nitride microdisk cavities. Appl Phys Lett 2013;103:021107.
[100] Zeng Y, Roland I, Checoury X, et al. Resonant second harmonic generation in a gallium nitride two-dimensional photonic crystal on silicon. Appl Phys Lett 2015;106:081105.
[101] Zeng Y, Roland I, Checoury X, et al. Imaging of photonic crystal localized modes through third-harmonic generation. ACS Photonics 2016;3:1240–7.
[102] Jung H, Stoll R, Guo X, Fischer D, Tang HX. Green, red, and IR frequency comb line generation from single IR pump in AlN microring resonator. Optica 2014;1:396–9.
[103] Sanford NA, Davydov AV, Tsvetkov DV, et al. Measurement of second order susceptibilities of GaN and AlGaN. J Appl Phys 2005;97:053512.
[104] Skauli T, Vodopyanov KL, Pinguet TJ, et al. Measurement of the nonlinear coefficient of orientation-patterned GaAs and demonstration of highly efficient second-harmonic generation. Opt Lett 2002;27:628–30.
[105] Xiong C, Pernice W, Ryu KK, et al. Integrated GaN photonic circuits on silicon (100) for second harmonic generation. Opt Express 2011;19:10462–70.
[106] Guo X, Zou C-L, Tang HX. Second-harmonic generation in aluminum nitride microrings with 2500%/W conversion efficiency. Optica 2016;3:1126–31.
[107] Painter O, Lee RK, Scherer A, et al. Two-dimensional photonic band-gap defect mode laser. Science 1999;284:1819–21.
[108] Lermer T, Gomez-Iglesias A, Sabathil M, et al. Gain of blue and cyan InGaN laser diodes. Appl Phys Lett 2011;98:021115.
[109] Sellés J, Crepel V, Roland I, et al. III-nitride-on-silicon microdisk lasers from the blue to the deep ultra-violet. Appl Phys Lett 2016;109:231101.
[110] Athanasiou M, Smith R, Liu B, Wang T. Room temperature continuous-wave green lasing from an InGaN microdisk on silicon. Sci Rep 2014;4:7250.
[111] Björk G, Yamamoto Y. Analysis of semiconductor microcavity lasers using rate equations. IEEE J Quantum Electron 1991;27:2386–96.
[112] Zhang Y, Ma Z, Zhang X, Wang T, Choi HW. Optically pumped whispering-gallery mode lasing from 2-μm GaN micro-disks pivoted on Si. Appl Phys Lett 2014;104:221106.
[113] Woolf A, Puchtler T, Aharonovich I, et al. Distinctive signature of indium gallium nitride quantum dot lasing in microdisk cavities. Proc Natl Acad Sci 2014;111:14042–6.
[114] Asada M, Miyamoto Y, Suematsu Y. Gain and the threshold of three-dimensional quantum-box lasers. IEEE J Quantum Electron 1986;22:1915–21.
[115] Strauf S, Hennessy K, Rakher MT, et al. Self-tuned quantum dot gain in photonic crystal lasers. Phys Rev Lett 2006;96:127404.
[116] Gong Y, Ellis B, Shambat G, Sarmiento T, Harris JS, Vučković J. Nanobeam photonic crystal cavity quantum dot laser. Opt Express 2010;18:8781–9.
[117] Rice PR, Carmichael HJ. Photon statistics of a cavity-QED laser: a comment on the laser-phase transition analogy. Phys Rev A 1994;50:4318–29.
[118] Choi YS, Rakher MT, Hennessy K, et al. Evolution of the onset of coherence in a family of photonic crystal nanolasers. Appl Phys Lett 2007;91:031108.
[119] Lohof F, Barzel R, Gartner P, Gies C. Delayed transition to coherent emission in nanolasers with extended gain media. Phys Rev Appl 2018;10:054055.
[120] Stegmaier M, Ebert J, Meckbach JM, Ilin K, Siegel M, Pernice WHP. Aluminum nitride nanophotonic circuits operating at ultraviolet wavelengths. Appl Phys Lett 2014;104:091108.
[121] Piggott AY, Lu J, Babinec TM, Lagoudakis KG, Petykiewicz J, Vučković J. Inverse design and implementation of a wavelength demultiplexing grating coupler. Sci Rep 2014;4:7210.
[122] Piggott AY, Lu J, Lagoudakis KG, Petykiewicz J, Babinec TM, Vučković J. Inverse design and demonstration of a compact and broadband on-chip wavelength demultiplexer. Nat Photonics 2015;9:374–8.
[123] Minkov M, Savona V, Gerace D. Photonic crystal slab cavity simultaneously optimized for ultra-high Q/V and vertical radiation coupling. Appl Phys Lett 2017;111:131104.
[124] Mahler L, Tredicucci A, Beltram F, et al. Vertically emitting microdisk lasers. Nat Photonics 2009;3:46–9.

[125] Kneissl M, Teepe M, Miyashita N, Johnson NM, Chern GD, Chang RK. Current-injection spiral-shaped microcavity disk laser diodes with unidirectional emission. Appl Phys Lett 2004;84:2485–7.
[126] Feng M, He J, Sun Q, et al. Room-temperature electrically pumped InGaN-based microdisk laser grown on Si. Opt Express 2018;26:5043–51.
[127] Tabataba-Vakili F, Rennesson S, Damilano B, et al. III-nitride on silicon electrically injected microrings for nanophotonic circuits. Opt Express 2019;27:11800–8.
[128] Ellis B, Mayer MA, Shambat G, et al. Ultralow-threshold electrically pumped quantum-dot photonic-crystal nanocavity laser. Nat Photonics 2011;5:297–300.
[129] Takeda K, Sato T, Shinya A, et al. Few-fJ/bit data transmissions using directly modulated lambda-scale embedded active region photonic-crystal lasers. Nat Photonics 2013;7:569–75.
[130] Park H-G, Kim S-H, Kwon S-H, et al. Electrically driven single-cell photonic crystal laser. Science 2004;305:1444–7.
[131] Jeong K-Y, No Y-S, Hwang Y, et al. Electrically driven nanobeam laser. Nat Commun 2013;4:2822.
[132] Crosnier G, Sanchez D, Bouchoule S, et al. Hybrid indium phosphide-on-silicon nanolaser diode. Nat Photonics 2017;11:297–301.
[133] Nakamura S, Senoh M, Mukai T. Highly p-typed Mg-doped GaN films grown with GaN buffer layers. Jpn J Appl Phys 1991;30:L1708–11.
[134] Sizov DS, Bhat R, Heberle A, Song K, Zah C. Internal optical waveguide loss and p-type absorption in blue and green InGaN quantum well laser diodes. Appl Phys Express 2010;3:122104.
[135] Sizov DS, Bhat R, Zah C. Optical absorption of Mg-doped layers and InGaN quantum wells on c-plane and semipolar GaN structures. J Appl Phys 2013;113:203108.
[136] Purcell EM. Spontaneous emission probabilities at radio frequencies. Phys Rev 1946;69:681.
[137] Auffèves A, Gerace D, Gérard J-M, França Santos M, Andreani LC, Poizat J-P. Controlling the dynamics of a coupled atom-cavity system by pure dephasing. Phys Rev B 2010;81:245419.
[138] Romeira B, Fiore A. Purcell effect in the stimulated and spontaneous emission rates of nanoscale semiconductor lasers. IEEE J Quantum Electron 2018;54:2000412.
[139] Athavale SD, Economou DJ. Realization of atomic layer etching of silicon. J Vac Sci Technol B 1996;14:3702–5.
[140] Lu W, Lee Y, Gertsch JC, et al. In situ thermal atomic layer etching for sub-5 nm InGaAs multigate MOSFETs. Nano Lett 2019;19:5159–66.
[141] Andreani LC, Panzarini G, Gérard J-M. Strong-coupling regime for quantum boxes in pillar microcavities: theory. Phys Rev B 1999;60:13276–9.
[142] Khitrova G, Gibbs HM, Kira M, Koch SW, Scherer A. Vacuum Rabi splitting in semiconductors. Nat Phys 2006;2:81–90.
[143] Auffèves A, Besga B, Gérard J-M, Poizat J-P. Spontaneous emission spectrum of a two-level atom in a very-high-Q cavity. Phys Rev A 2008;77:063833.
[144] Tränhardt A, Ell C, Khitrova G, Gibbs HM. Relation between dipole moment and radiative lifetime in interface fluctuation quantum dots. Phys Rev B 2002;65:035327.
[145] Reparaz JS, Chavez-Angel E, Wagner MR, et al. A novel contactless technique for thermal field mapping and thermal conductivity determination: two-laser Raman thermometry. Rev Sci Instrum 2014;85:034901.
[146] Chávez-Ángel E, Reparaz JS, Gomis-Bresco J, et al. Reduction of the thermal conductivity in free-standing silicon nano-membranes investigated by non-invasive Raman thermometry. APL Mater 2014;2:012113.
[147] Fan L, Sun X, Xiong C, Schuck C, Tang HX. Aluminum nitride piezo-acousto-photonic crystal nanocavity with high quality factors. Appl Phys Lett 2013;102:153507.
[148] Tadesse SA, Li H, Liu Q, Li M. Acousto-optic modulation of a photonic crystal nanocavity with Lamb waves in microwave K band. Appl Phys Lett 2015;107:201113.
[149] Yu Z, Fan S. Complete optical isolation created by indirect interband photonic transitions. Nat Photonics 2009;3:91–4.
[150] Bochmann J, Vainsencher A, Awschalom DD, Cleland AN. Nanomechanical coupling between microwave and optical photons. Nat Phys 2013;9:712–6.
[151] Shambat G, Kothapalli S-R, Provine J, et al. Single-cell photonic nanocavity probes. Nano Lett 2013;13:4999–5005.
[152] Gutierrez Herrera C, Carus Cadavieco M, Jego S, Ponomarenko A, Korotkova T, Adamantidis A. Hypothalamic feedforward inhibition of thalamocortical network controls arousal and consciousness. Nat Neurosci 2016;19:290–8.
[153] Warden MR, Cardin JA, Deisseroth K. Optical neural interfaces. Annu Rev Biomed Eng 2014;16:103–29.
[154] Berndt A, Schoenenberger P, Mattis J, et al. High-efficiency channelrhodopsins for fast neuronal stimulation at low light levels. Proc Natl Acad Sci U S A 2011;108:7595–600.

**Supplementary Material:** The online version of this article offers supplementary material (https://doi.org/10.1515/nanoph-2019-0442).